Miguel Alexandre Pinheiro Candeias Cruchinho Carreto

Licenciado em Engenharia de Materiais

Tuning Photonic Properties of Cellulose-Clay Nano Structures

Dissertação para obtenção do Grau de Mestre em
Engenharia de Materiais

Orientadora: Doutora Ana Catarina Rodrigues Trindade, Postdoctoral Researcher, Faculdade de Ciências e Tecnologia da Universidade Nova de Lisboa

Co-orientadora: Professora Doutora Maria Helena Godinho, Associated Professor with Agregation, Faculdade de Ciências e Tecnologia da Universidade Nova de Lisboa

FACULDADE DE CIÊNCIAS E TECNOLOGIA
UNIVERSIDADE NOVA DE LISBOA

Outubro, 2019

Tuning Photonic Properties of Cellulose-Clay Nano Structures

Copyright © Miguel Alexandre Pinheiro Candeias Cruchinho Carreto, Faculdade de Ciências e Tecnologia, Universidade Nova de Lisboa, 2019.

A Faculdade de Ciências e Tecnologia e a Universidade Nova de Lisboa têm o direito, perpétuo e sem limites geográficos, de arquivar e publicar esta dissertação através de exemplares impressos reproduzidos em papel ou de forma digital, ou por qualquer outro meio conhecido ou que venha a ser inventado, e de a divulgar através de repositórios científicos e de admitir a sua cópia e distribuição com objetivos educacionais ou de investigação, não comerciais, desde que seja dado crédito ao autor e editor.

Acknowledgements

Em primeiro lugar quero agradecer à minha orientadora, Doutora Ana Catarina Rodrigues Trindade que me prestou toda a sua atenção, paciência e boa disposição. À minha co-orientadora, Professora Doutora Maria Helena Godinho por me ter acompanhado ao longo do meu percurso académico e por todo o conhecimento incrível que me transmitiu. Quero agradecer à Doutora Susete Fernandes por me ter despertado o interesse pelo mundo da celulose, pelo auxilio com a produção de CNCs e pela disponibilidade para responder às minhas questões. Ao Diogo Saraiva e Ricardo Chagas deixo um grande obrigado, pois sempre me ajudaram a resolver todos os problemas e me retiraram todas as dúvidas necessárias. Um obrigado também aos restantes membros do grupo de investigação do laboratório.

Quero também agradecer ao Professor Doutor Josef Breu e ao seu grupo da Universaidade de Bayreuth por ter cedido as Clays e ao Professor Doutor Jon Otto Fossum pela disponibilidade e esclarecer dúvidas e ajudar com ideias em relação às clays.

Agradeço à minha família por me terem apoiado e ajudado, mesmo quando não percebiam da matéria em questão. Obrigado ao meu tio por todas as explicações de matemática. Agradeço-vos pela paciência incondicional.

Quero deixar um grande obrigado à minha namorada Beatriz que me acompanhou ao longo deste longo e difícil caminho e por toda a paciência que teve comigo. Não posso deixar de agradecer aos meus amigos (não vou enumerar porque ainda me esqueço de alguém). Todos vocês foram imprescindíveis ao longo destes anos.

Por último não posso deixar de agradecer aos que me acompanharam durante estes meses dedicados à investigação: Margarida, Bárbara, Adriana, César, Ana Sofia e Lavadinho. Passámos pelo melhor e pelo pior juntos, mas o mais importante foi a entreajuda entre nós. Deixo um obrigado especial à Rita que foi uma pessoal fundamental durante todo o meu percurso académico e que será uma amiga para a vida.

Este trabalho foi financiado por fundos concedidos pela FEDER através do Programa COMPETE 2020, Fundos Nacionais, através da FCT – Fundação para a Ciência e Tecnologia e também pelo POR Lisboa2020 ao abrigo dos projetos POCI – 01-0145-FEDER-007688 (Referenciar UID/CTM/50025) e PTDC/CTM-REF/30529/2017 (NanoCell2SEC), e também da rede M-ERA.NET pelo projeto com referência M-ERA-NET2/0007/2016 (CellColor).

Resumo

A cor estrutural é um fenómeno ótico fascinante, que varia com o ângulo de observação (iridescente), que pode ser observada em animais (por exemplo: penas dos pavões), bem como em plantas (por exemplo: bagas da planta *Pollia condensata*). Este fenómeno ocorre devido à interação da luz com as estruturas periódicas à nanoescala, produzindo desta forma cores muito vivas. Simular estas cores iridescentes com materiais naturais é um dos principais objetivos deste trabalho.

De fato, após a evaporação do solvente, as suspensões aquosas de celulose nanocristalina (CNCs) podem ser utilizadas para produzir filmes sólidos iridescentes. Estes filmes têm uma estrutura helicoidal que roda à esquerda, que reflete a luz circularmente polarizada à esquerda (LCP) e transmite a luz circularmente polarizada à direita (RCP). Por outro lado, as partículas de nano argilas podem apresentar organizações periódicas lamelares no estado sólido, enquanto suspensões aquosas da argila biaxial “sodium-fluorohectorite” (NaFh) podem formar fases líquidas cristalinas nemáticas uniaxiais. Foi utilizada uma outra nano argila, cesium double layer (Cs-Ds). Neste trabalho, as CNCs e as nano argilas foram utilizados para desenvolver superfícies nanoestruturadas amigas do ambiente e com funcionalidade ótica para coloração e reflexão da luz.

De modo a estudar o comportamento ótico obtido a partir da solução aquosa de CNCs misturadas com partículas de NaFh, com várias razões de CNCs/argila, foram depositadas gotas das soluções em diferentes substratos e o solvente foi evaporado sob diferentes condições. Os filmes finos obtidos foram caracterizados por diferentes técnicas de caracterização e comparados, de modo a selecionar a melhor razão celulose/argila e as condições a serem utilizadas na preparação de filmes sólidos. O diagrama de fases do sistema CNCs/NaFh também foi obtido.

Os filmes finos e os filmes sólidos preparados apresentam iridescência. É possível ajustar as propriedades fotónicas destes filmes iridescentes: com o aumento da concentração de argila os filmes apresentam uma transição de coloração refletida de azul para verde do espetro da luz visível.

Palavras-chave: Celulose Nanocristalina, Partículas de nano argila, Sodium-Fluorohectorite (NaFh), Filmes sólidos de CNCs/argila, Propriedades fotónicas, argilas de mono e dupla camada, nano argilas sintéticas.

Abstract

Fascinating structural colors, which varies with the angle of observation (iridescent) can be seen in animals (ex: feathers of the peacock), as well as in plants (ex: *Pollia condensata* berries). These colors are very vivid and remain in time due to periodic structures at the nanoscale, which are at their origin. Mimicking these iridescent colors with natural materials is one of the main targets of this work.

In fact after, solvent evaporation, aqueous suspensions of cellulose nanocrystals (CNCs) can be used to produce iridescent solid films. These films have a left-hand helicoidal structure, which reflects left circularly polarized (LCP) light and transmits right circularly polarized (RCP) light. On the other hand nanoclay particles can present lamellar periodic organizations in the solid state, while aqueous suspensions of sodium-fluorohectorite (NaFh) clay biaxial platelets can form nematic uniaxial liquid crystalline phases. In addition, another nanoclay, Cesium double layer (Cs-Ds), was also used. In this work CNCs and nanoclays were used to develop environmentally friendly nanostructured surfaces with engineered optical functionality for coloration and reflection of light.

In order to study the optical behavior of CNCs mixed with NaFh particles aqueous solutions, with various CNCs/Clay ratios, were dropwise in different substrates and the solvent was allowed to evaporate under different conditions. The thin films, prepared by drop-casting method, were characterized by different techniques and then set side by side, with the intention of selecting the best ratio and conditions to be used in the preparation of solid films by solvent evaporation method in Petri dishes. The phase diagram of the system NCC/NaFh was also obtained.

The thin films as well as the solid films prepared show iridescence. It is possible to adjust the photonic properties of these solid iridescent films: a green shift was obtained for higher concentration of clay.

Keywords: Cellulose Nanocrystals (CNCs), Nanoclay particles, Sodium-Fluorohectorite (NaFh), CNCs/clay solid films, Photonic properties, Mono and double layer Clays, Synthetic Nanoclays

Table of contents

List of figures

List of Tables

Acronyms

AFM	Atomic Force Microscopy
ATR	Attenuated Total Reflectance
$C_6H_{10}O_5$	Cellulose
Ch	Cholesteric
CrI	Crystallinity Index
CMC	Microcrystalline Cellulose
CMF	Cellulose Microfibril
CNCs	Cellulose Nanocrystals
Cs-Ds	Cesium Double Layer
$\overline{DP}$	Degree of Polymerization
DS	Degree of Substitution
DSC	Differential Scanning Calorimetry
EA	Elemental Analysis
FTIR	Fourier Transform Infrared
FWHM	Full Width at Half Maximum
H_2SO_4	Sulfuric Acid
ITO	Indium Tin Oxide
LC	Liquid Crystal
LCP	Left Circularly Polarized
N	Nematic
n	Director
$\bar{n}$	Average Refractive Index
NaFh	Sodium Fluorohectorite
P	Pitch
POM	Polarized Optical Microscopy
RCP	Right Circularly Polarized
SEM	Scanning Electron Microscopy
TGA	Thermogravimetric Analysis

UVO	Ultraviolet Ozone
XRD	X-Ray Diffraction
λ	Reflected Wavelength

1 Motivation

Today we live in a world where color is vastly present in our day to day life throughout the use of paint. Paint can be used as a decorative element, protection against environmental conditions, amongst other applications. Some of its constituents are: pigments, binder, extender, solvent and additives. These pigments provide the coloration and opacity to the paint while being practically insoluble in the substance in which they are incorporated [1].

Pigments are subdivided into two main source classifications: organic and inorganic. The organic ones were used in the past and were made out of natural sources, however nowadays the most common are inorganic and synthetic-organic. Inorganic pigments are made out of chemicals that are toxic to humans, animals and the environment. Synthetic organic pigments are the latest type and they are mainly derived from phthalocyanines or azo compounds amongst other harmful chemical compounds.

Although the pigments used today are less toxic and destructive to the environment, they are still prejudicial. Therefore, the demand to industrially produce an alternative non-toxic, economical viable and environmentally friendly pigments is rising.

Cellulose nanocrystals (CNCs) particles are a nanomaterial produced from cellulose with numerous benefits: they are widely available, renewable, inexpensive, environmentally friendly, biocompatible and nontoxic. An aqueous suspension of CNCs forms a chiral nematic phase above a certain critical concentration due to the CNCs rod-like shape. CNCs solid films, produced by solvent evaporation, exhibit iridescence and have a left-hand helicoidal structure, which reflects left circularly polarized (LCP) light and transmits right circularly polarized (RCP) light [2].

Clay minerals are naturally inexpensive and abundant. They are vastly used in many applications (ex: industrial, agricultural, including others). Nanoclays are nanoparticles of layered mineral silicates and can be subdivided in different classes such as: kandite, illite, smectite and vermiculite. Specific smectite nanoclays (ex: Sodium-Fluorohectorite) when in an aqueous suspension display a nematic phase.

The aim of this work is to obtain solid films with optical functionality for coloration and selective reflection of light, taking inspiration from natural structural coloration seen in animals and plants. The iridescent films will be produced from environmentally friendly, nano-structured, cost effective and sustainable natural materials, such as cellulose and clays. The following objectives were proposed, in order to achieve this ambition:

- Evaluate the impact of thin films from CNCs/Clay suspensions prepared with different evaporation temperatures and deposition substrates;
- Evaluate the optical response of thin films from different percentages of CNCs mixed with NaFh;
- Assess the difference in optical response of solid films from CNCs, CNCs mixed with two different nanoclays, a monolayer and a bi-layer
- Characterize the solid films with several techniques.

This work's structure is divided in four mains parts: the first part focuses on a theoretical introduction of the state of the art; secondly the materials and methods used are described; the third part will contain all the results, which will be thoroughly discussed; and at the end the conclusions are reported and future perspectives are suggested.

2 Introduction

2.1 Structural Color

Nature is an inexhaustible source of inspiration for materials science due to evolution and natural selection. Life on earth has developed extraordinary complex multifunctional molecules and materials with unique properties. Natural creatures have established distinctive functions such as directional water collection on wetted spider silk, antifogging properties of mosquito compound eyes, water capture and wing-locking device of the beetle, multicolor of butterfly wings, super hydrophobicity and low adhesion of lotus leaf, among other examples [3].

In recent years, structural colors have attracted much attention in a wide variety of research fields due to the complex interactions between light and sophisticated microstructures created in the natural world [4]. This mechanism forms the basis of the most stunning displays of color in nature that can be observed in butterflies, moths, beetles, birds, fishes, plants and fruits, some examples illustrated in Figure 2.1. A great example of this type of coloration can be found on the *Morpho* butterfly wings, which occurs due to the presence of lamellar structures in its ridges, that offer a strong reflection in a given wavelength [5].

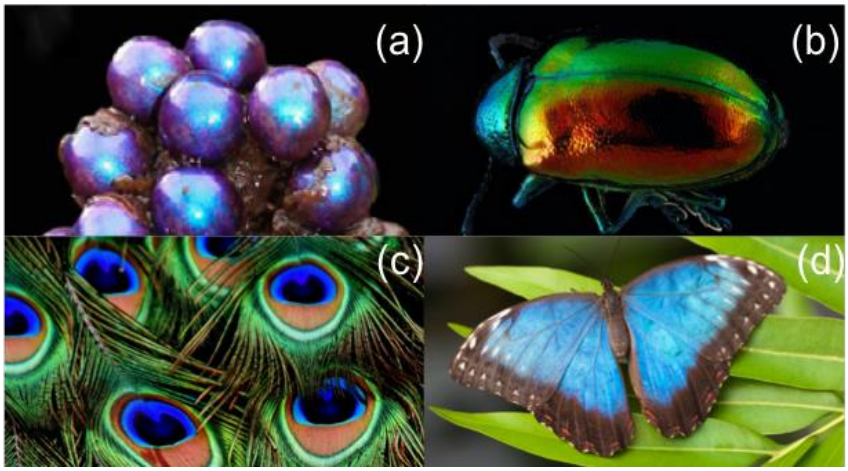

Figure 2.1 – Examples of structural colors in nature: (a) *Pollia condensata* [6]; (b) Dogbane beetle [7]; (c) Peacock feathers [8]; (d) Blue *Morpho* butterfly [9].

2.2 Cellulose

The depletion of petroleum-based resources and the attendant environmental problems, such as global warming, have stimulated considerable interest in the development of environmentally sustainable materials. Bio-based materials have various advantages (renewability, biodegradability, and environmental friendliness) and can be used as suitable as a means of overcoming environmental problems. Cellulose, $[C_6H_{10}O_5]_n$ the most abundant renewable organic compound on earth, is a fascinating and almost inexhaustible sustainable natural polymer that has been vastly used in our day-to-day products and applications and considered an alternative to fossil fuel-based polymers [10], [11]. Other advantages are its availability, low cost, low density, nontoxicity, low abrasiveness, biocompatibility and biodegradability and are currently used in a wide range of fields such as the automotive and construction industries, electronic components, sports and leisure, etc. [11].

More recently, cellulose was found to be an ideal environmentally friendly material to mimic periodic micro and nanostructure that produce iridescence and structural coloration [12]. Pinto *et al.* reported on a new type of liquid crystalline cellulosic films with light controllable reversible wettability [13]. The authors combined, at room temperature, the light responsive properties of azo compounds with cellulosic liquid crystalline materials, therefore opening new opportunities in surface engineering using eco-friendly cellulose manipulation.

Cellulose is fibrous, tough, water-insoluble and can be found in the cell wall of plants, algae, bacteria and some sea animals, as in tunicates [14]. The repeating unit of cellulose, is cellobiose, illustrated in Figure 2.2 (a), and consists of β glucose units that are alternately inverted at a 180° angle forming a main chain polymer, via 1,4 glycosidic bonds formed by a condensation reaction. The chains are stabilized laterally by hydrogen bonds forming microfibrils, which are grouped in crystalline and disordered regions as schematically shown in Figure 2.2 (b). These microfibrils are assembled into macrofibers and fibers forming self-assembled hierarchical structures [15]. The average degree of polymerization ($\overline{\mathrm{DP}}$) differs for each different source of cellulose, as for example the cellulose extracted from wood has a $\overline{\mathrm{DP}}$ of 10.000 and the one from wool has a $\overline{\mathrm{DP}}$ of 15.000 [14].

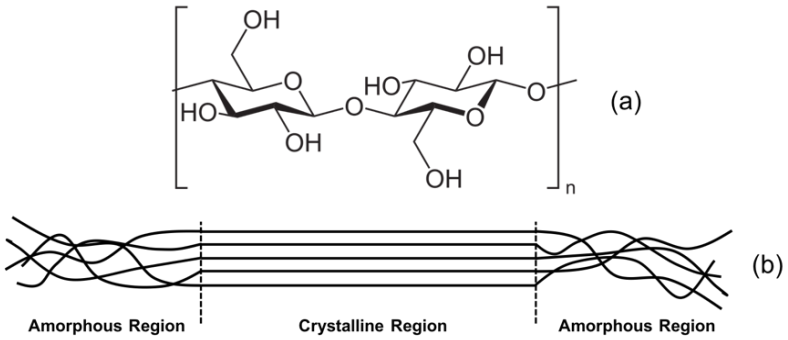

Figure 2.2 – (a) Chemical structure representation of cellulose repetitive unit, cellobiose [16] and (b) Cellulose chain with both amorphous and crystalline regions.

The progress of nanotechnology in parallel with attention to bio-based materials using cellulose, sparked interest in nanocellulose. By reducing to the nano-scale, nanocellulose wider the range of applications in which cellulose is used. Nanocellulose are produced by removing the amorphous regions of the main chain, leaving mostly the crystalline regions intact, Figure 2.2 (b), and have many advantages including stiffness combined with low weight, very high surface area-to-volume ratio, high aspect ratio, impressive mechanical properties (Nano strength), biodegradability and thus also being possible its use as reinforcement [11].

Depending on the preparation method, shape, dimension and function it is possible to obtain different types of nanocellulose structures. The raw fibers need to go through a specific pretreatment process in order to eliminate lignin and hemicellulose present in this raw state and to isolate purified cellulose [17]. The pretreatment processes used in this process need to be chosen accordingly to the cellulose source and to the desired morphology. The prime pretreatments are, usually, pulping, bleaching, oxidation or enzymatic processes.

After the initial purification the obtained fibers can go through a specific process in order to either obtain cellulose microfibrils (CMFs) or cellulose nanocrystals (CNCs) [14]. Rojas and co-workers obtained *Eucalyptus* cellulose micro/nanofibers through three different processes, namely: refining; sonication; and acidic hydrolysis of the cellulosic pulp [18]. They showed that, by using mechanical and chemical processes, the micro/nanofibers can be isolated.

In this work, it will only be exploited the use of cellulose nanocrystals, which synthesis and characteristics will be revealed in the next paragraph.

2.3 Cellulose Nanocrystals (CNCs)

By exploit cellulose at the nanoscale, a next generation of multifunctional polymer nanocomposites can be obtained by employing a new cellulose-based “building block” known as nanocellulose [11]. Nanocellulose erns a number of advantages such as high aspect ratio, low density (1.6 g cm^{-3}), and a reactive surface of –OH side groups that facilitate the attachment of desired functional groups onto these nanocellulose surface to achieve different surface properties.

As previously stated the cellulose nanocrystals are produced by removing the amorphous domains (see Figure 2.2 (b)) through a controlled chemical treatment, usually a strong acidic hydrolysis with temperatures above room temperature, followed by high-power mechanical or ultrasonic treatments and neutralizations with distilled water, in order to remove free acid from the dispersion [17]. The geometric dimensions of CNCs, such as length and width, vary depending on the origin of cellulose microfibrils and the acidic hydrolysis conditions (such as time and temperature), cellulosic source [10]. CNCs have remarkable mechanical properties and, so, potential applications in many areas, including materials science, electronic and/or medicine [10], [19].

The extraction of CNCs using acidic hydrolysis results in a suspension consisting of nanorods [20]. Above a critical concentration and under suitable conditions, CNCs self-assemble in the suspension and form a chiral nematic liquid crystalline phase, as a result of their rod-like shape (illustrated in Figure 2.3) [21]. Beck-Candanedo *et al.* mentioned Rånby and Ribi in the production of stable suspensions of colloidal-sized cellulose crystals by sulfuric acidic hydrolysis of wood and cotton cellulose in 1949 [22].

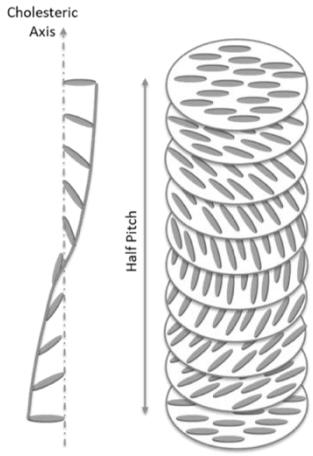

Figure 2.3 – Schematic representation of chiral nematic order displayed by cellulose nanorods.

Solid films prepared from CNCs present remarkable optical properties: iridescence, selective reflection of left circularly polarized light, and transmission of right circularly polarized light [23]. Fernandes *et al.* found that the mechanical and optical properties of micrometer thin transparent cellulosic films can be tuned by modifying the precursor liquid crystalline characteristics of the system and by adding CNCs [24]. They reported sheared iridescent cellulosic films, with tunable mechanical and structural color properties, which mimic the structures found in petals of some flowers.

Liquid crystals (LCs) represent a state of matter between the solid and the liquid, which combines the optical properties of crystals, birefringence, with the mechanical properties of liquids. LCs present different structures being the nematic (N), the smectic (Sm) and the cholesteric (Ch, N*) the most referred in literature [25].

In the nematic structure, there are no layers and the molecules show long orientational order along a preferential orientation (the director (**n**)) and no positional order [26].

Cholesteric or nematic chiral structures consist of pseudo layers of molecules aligned along with **n**, with the orientation of each director rotated, about the cholesteric perpendicular axis, from one layer to the next, as represented schematically in Figure 2.3 [27]. The distance in which the director rotates a full turn of 360º is normally designated by pitch (P) [11], which is in the range of 0.4–0.8 μm (corresponding to the visible light range).

A chiral nematic structure whose pitch (P) is of the order of the wavelength of visible light reflects circularly polarized light, and the reflected light wavelength changes with the viewing angle, leading to an iridescent appearance [28]. The dependence of the value of the wavelength reflected by the cholesteric structure with the angle of incidence is given by the *de Vries* equation:

$$\lambda = nP \sin\theta \qquad \text{Equation 1}$$

In Equation 1 θ represents the angle of light incidence, λ the reflected wavelength by the sample, $\bar{n}$ the average refractive index of the sample ((cholesteric (chiral nematic)) phase and P the value of helical pitch [29]. The pitch, defined by the distance required for the director to complete a full turn is a function of both the temperature and concentration [2].

The director of each consecutive layer, of the chiral nematic structure of CNCs, is rotated left-handed, which means that the left circularly polarized (LCP) light is reflected by the CNCs structure. In fact, right circularly polarized (RCP) light is reflected by cholesterics with a right-handed helix, while left circularly polarized (LCP) light is reflected by cholesteric materials with a left-handed helix [24]. Godinho and co-workers reported a cellulose-based photonic structure, which reflects both RCP and LCP light that can be tuned by temperature variation and the application of an external electric field [23].

2.4 Clay

There is presently a growing scientific activity associated with including clays into modern materials science together with other synthetic and complex adaptive materials such as colloids, polymers, liquid crystals and bio materials [30]. Clays are fascinating materials present almost everywhere on Earth and, although clays have been studied for centuries by geologists and geochemists, the fundamental study of some complex physical phenomena in clays is a relatively new field [31].

Liu *et al.* combined montmorillonite clay and cellulose nanofibrillated to prepare clay nanopaper hybrid for fire retardancy and gas barrier functions [32]. They added montmorillonite in order to improve the barrier properties of pure cellulose nanopaper. The data suggest that clay nanopaper is of great interest for application in self-extinguishing composites and for further development into barrier layers in packaging applications.

Due to their abundance, availability and inexpensive price, clay minerals have been used in agricultural applications, engineering and construction applications, environmental remediation, geology, pharmaceuticals, food processing, and many other industrial applications [33]. Clay minerals are phyllosilicates, which are made up of by sheet structures based on the Si_4O_{10} unit cell. There are two types of sheets: a tetrahedral sheet, which is made up of silicon-oxygen tetrahedrons with shared basal oxygen molecules (T layer), and a octahedral sheet, which is made up of aluminium-oxigen octahedrons with shared apical and basal oxygen (O layer) [34], Figure 2.4.

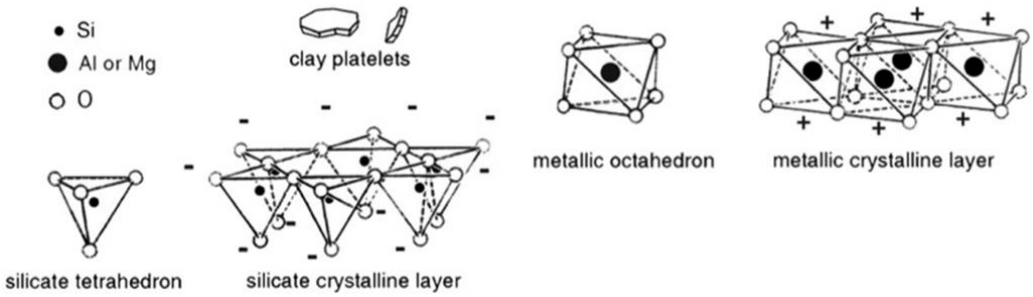

Figure 2.4 – Representation of a tetrahedral sheet, a octahedral sheet and the corresponding T and O layers, [68].

Bonding one tetrahedral sheet with one octahedral sheet results in the formation of 1:1 clay, on the other hand when two tetrahedral sheets are bonded with a single octahedral sheet, 2:1 clay is formed [35]. These clay layer structures can be observed in Figure 2.5.

The 1:1 clay minerals are electrically neutral therefore they will not attract charged species and do not swell in water. The 2:1 clay minerals are negatively charged and able to swell in water, therefore the water molecules infiltrate between the layers [36].

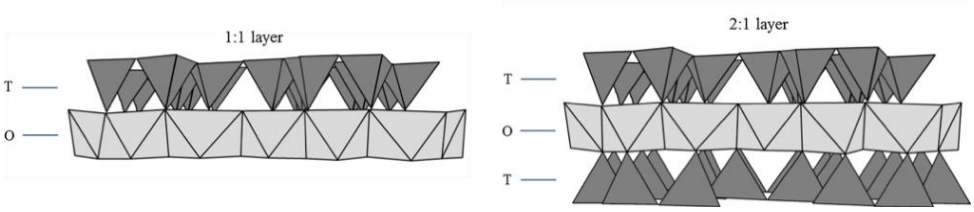

Figure 2.5 – Representation of 1:1 and 2:1 clay layer structures: O and T refer to octahedral and tetrahedral layers, respectively, [69].

2.5 Nanoclay

The combination of chemical and physical properties of various layered materials allows for the assembly of ordered heterostructures with tailored optical and electronic properties [37].

There are four major groups of clay minerals: kandite, illite, smectite and vermiculite [33]. Sodium-Fluorohectorite (NaFh), with nominal composition of $[Na_{0.5}]^{inter}[Mg_{2.5}Li_{0.5}]^{oct}[Si_4]^{tet}O_{10}F_2$, is a smectite clay, that belongs to the 2:1 clay family and when in the dry state the layers are stacked like a deck of cards [38], [30]. Sodium-Fluorohectorite is a water swelling clay that when in contact with water incorporates a variable amount of it in the interlayer space, resulting in a change in the lattice constant along the stacking direction [39]. The superior charge homogeneity of this material allows for swelling and quantitative delamination into individual platelets and that´s why it is usually known as a monolayer clay.

The counterion present in the interlayer space, that balances the charges and allow the layers to be stacked, is the cation Na^+ [40]. Furthermore, these particle stacks can swell more in the presence of water, increasing the distance between the layers and delaminate, [41], as shown in Figure 2.6.

Synthetic Na-hectorite belongs to a handful of layered compounds that show the long-known but rare phenomenon of osmotic swelling [42]. Contrary to liquid-phase exfoliation typically applied e.g. with graphene, that applies brute force sonication, osmotic swelling is a thermodynamically allowed process [43]. It allows for an utter and most gentle delamination preserving the aspect ratio inherent in the tactoid diameter of the starting material. For Na-hectorite, nanosheets

with a thickness of 1 nm and a median diameter of 20 µm are obtained simply by immersing the clay as synthesized material into deionized water. Due to the large aspect ratio even very dilute suspensions (< 1% vol) are not isotropic but rather nematic.

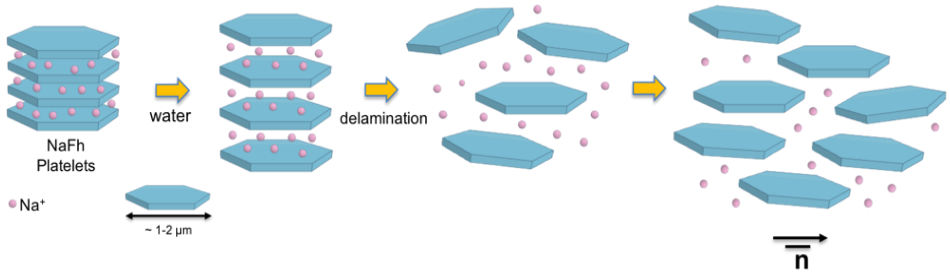

Figure 2.6 – Swelling and delamination of the monolayer NaFh nanoclay

Like reported for titanate nanosheets, dilute aqueous dispersions of Na-hectorite nanosheets adopt a cofacial arrangement due to strong electrostatic repulsion and exhibit structural colors. In this nematic state adjacent silicate layers are not only held in a coherent cofacial geometry but are also separated to long distances which are determined by the clay content and typically exceed 50 nm. This allows for easy diffusion of polymer chains into the spacious galleries between adjacent layers. Simply by mixing the aqueous nematic clay dispersions with polymer solutions perfectly homogeneous nanocomposites can be obtained.

Colloidal suspensions of NaFh synthetic clay platelets in a NaCl solution, exhibit coexisting isotropic and nematic phases. The NaFh suspensions leads to four distinct coexisting phases which are, from bottom to top: isotropic flocculated sediment (FS), nematic gel (NG), nematic sol (NS), and isotropic sol (IS) [44]. The nematic gel displays a translucent texture, because it has particles with a preferred direction of orientation [41].

Hemmen *et al.* studied the ordering of Na-fluorohectorite synthetic clay platelets at the interfaces between various coexisting phases [31]. They used different experimental techniques, in order to determine the type of order prevailing in each phase and at the interfaces. With the results obtained, they were able to produce a schematic illustration of the order most likely prevailing in the nematic gel and nematic sol regions.

In the end of this work it was used a cesium double layer synthetic clay (Cs-Ds), from the same group as the NaFh. The objective was to compare the results obtained with different clays. However, this clay was recently synthetized by Breu group in Bayreuth and there are no bibliography about that, as studies and characterization is still on going and un-published. In Figure 2.7 is represented a schematic representation of swelling and delamination of Cs-Ds nanoclay, where it is visible the intercalation of a cationic molecule of Cs in the synthetic layered silicates.

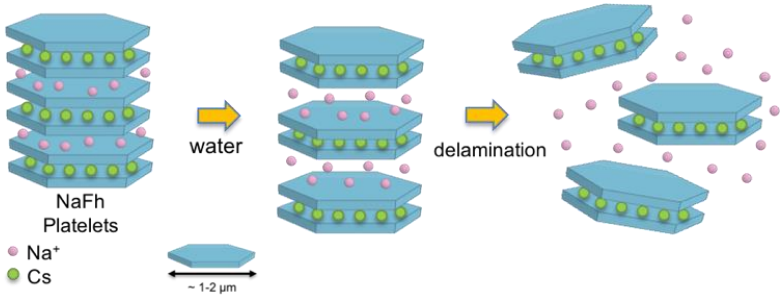

Figure 2.7 – Swelling and delamination of Cs-Ds nanoclay.

The swelling of this double layer clay originates, as its name suggest, not single layers of nanoclays, but double layers in which the sodium fluorohectorite platelets are attached one to another by the Cs ion (Cs^+).

3 Materials and Methods

3.1 Materials and isolation techniques

3.1.1 CNCs isolation

The CNCs particles were prepared based on the method documented by Gray and co-workers [45], with minor adjustments by Fernandes et al. [23].

The cellulosic source used in this work is a commercial microcrystalline cellulose derived from cotton and acquired from Sigma-Aldrich (CMC; Avicel®, PH-101, ~ 50 µm particle size, lot #BCBJ0229V). Microcrystalline Cellulose was hydrolyzed in sulfuric acid, H_2SO_4, (95% - 97% purity, Sigma-Aldrich), with an acid concentration of 64% (w/w), an acid/solid ratio of 8.5:1, at 45 ºC for 40 minutes, under continuous magnetic agitation. In order to cease the reaction, ultrapure water (Millipore Elix Advantage 3 water purification systems) was added, with a volume of 10 times the initial volume of the reaction. The resulting material was washed, diluted and centrifuged with ultrapure water (12 000 rpm for 20 minutes, Thermo Scientific Heraeus Multifuge X1R Centrifuge Series) until the pH of the CNCs suspension was between 1.9 – 3.9 and then the supernatant was collected. The suspension was dialyzed in ultrapure water (using Spectrum Spectra/Por® 4 dialysis membranes), and the water was changed every day, until constant pH readouts were obtained. The suspension was produced by submitting it to 3 consecutive cycles of 20 minutes of sonication (Hielscher UP400S ultrasonic homogenizer, 460 W, 24 kHz) over an ice bath at 0.85 of the cycle and 80% amplitude. The concentration of the produced aqueous CNCs suspension, obtained by gravimetry, was 2.47% (w/w).

3.1.2 Nanoclays

Throughout the work two different types of nanoclays were used, Sodium Fluorohectorite (NaFh) and Cesium double layer (Cs-Ds). These nanoclays were obtained through a collaboration with Prof. Dr. J. Breu group, from the University of Bayreuth in Germany. The studies in this work were mostly performed with sodium Fluorohectorite nanoclay for the fabrication of thin films and solid films. In the other hand, the Cs-Ds nanoclay was only used later in the work, for the preparation of solid-state films, to compare with the first ones prepared with NaFh.

NaFh is a synthetic nanoclay, as said before, that was synthetized by melt synthesis in a gastight molybdenum crucible, based on the documented procedure by Breu *et al.* [46], [47]. This nanoclay was provided in the solid state, but in this work, it was used a suspension in ultrapure water with a nanoclay concentration of 1% (w/w). The suspension was prepared by diluting the nanoclay, until the desired concentration was achieved. The fully delamination was achieved by leaving overnight the sample in ultrapure water.

The Cs-Ds nanoclay was provided in a suspension state. The solution was diluted to the required values in order to achieve the intended mixing ratios of CNCs and Cs-Ds.

3.1.3 CNCs/Clay mixtures and Phase Diagram

Firstly using aqueous suspension of NaFh, 1% (w/w) concentration, and the aqueous CNCs suspension, 2.47% (w/w) concentration, five mixtures with different percentages were prepared 99% CNCs 1% NaFh (w/w); 98% CNCs / 2% NaFh (w/w); 95% CNCs / 5% NaFh (w/w); 85% CNCs with 15% NaFh (w/w); 50% CNCs / 50% NaFh (w/w).

The phase diagram was made by using the mixtures suspensions, described before, with the same different ratios that would be used to drop-cast thin films. Each mixture was placed in a

vial (VWR™, 1.5 ml) and was left to rest for at least 1 month, in a cold atmosphere of 4 ºC, until phase separation (isotropic and anisotropic phases) was visible.

3.1.4 Thin films from droplets and casting solid films

Droplets, with 10 µl, of each mixture (for each temperature) were drop-casted using a Easy 40+ micropipette in order to produce thin films, by solvent evaporation process. Three different temperature conditions (4 ºC, 20 ºC and 60 ºC) and two different substrates were tested. The first substrate used was 100 Ω/sq Indium Tin Oxide (ITO) coated square glass substrates (15x15x0.7 mm) and the second was microscope slides (VWR™, 76x26x1 mm). The ITO substrate was, previously to the droplet deposition, exposed to UV light and Ozone (O_3), using a Novascan PSD-UV.

CNCs/Clay solid films were produced, by solvent evaporation method, by depositing the different mixtures ratios onto polystyrene Petri dishes (with 35 mm in diameter), with a volume of 2 ml with an evaporation temperature of 4 ºC. The solid films were left untouched until complete evaporation of the solvent.

3.2 Characterization

Atomic Force Microscopy (AFM) allowed to determine the average dimensions of length and width of the CNCs, by means of an Asylum Research MFP-3D Stand Alone in tapping mode with commercial silicon probes (scanning frequency of 300 kHz, k=26 N/m). The samples to be characterized were submitted to a preparation process, consisting in sonication (using a Hielscher UP400S, 460 W, 24 KHZ, at 0.85 of the cycle and 80% amplitude) of a diluted aqueous CNCs suspension, 0.01% (w/w), on an ice bath during two consecutive runs of 10 minutes. Immediately after the sonication process a droplet with 1 µl, of the diluted suspension, was deposited onto a mica substrate (Muscovite Mica V-5 from Electron Microscopy Sciences). The acquired AFM images were analyzed via the software Gwyddion (version 2.53, http://gwyddion.net), which consisted in 150 manual measurements of length and width of the CNCs particles.

Elemental analysis (EA) was conducted by the elemental analyzer Flash EA 1112 CHNS series from Thermo Finnigan-CE Instruments. The analyzer operation is based on the dynamic combustion method of vanadium peroxide catalyzed material and is fully operated by a computer software, which generates a full report of the sample in CHNS (in percentages between 0.01% and 100%).

Fourier Transform Infrared (FTIR) spectroscopy was used to chemically characterize microcrystalline and nanocrystalline cellulose used throughout this work. For this characterization it was used the spectrometer Spectrum Two FTIR Spectrometer, equipped with an attenuated total reflectance (ATR) (Perkin Elmer Ltd, Bucks, UK), with a spectral gap from 4000 to 400 cm^{-1} and a resolution of 4 cm^{-1}, at room temperature.

X-Ray Diffraction (XRD) spectra was conducted using a X-Ray diffractometer (PANalytical XPert PRO MRD), with Bragg-Brentano (θ/2θ coupled) with CuK (1.5406 Å) radiation, with 45 KV and 40 mA. The specification for the scanning step, during the characterization, was 2θ=0.0334, from 10^o to 40^o.

Using the thermal analyzer NETZSCH STA 449 F3 Jupiter® the differential scanning calorimetry with thermogravimetric analysis (DSC-TGA) was performed. The specifications used, to determine the caloric effects and mass change, the samples were heated from 25 ºC to 550 ºC at a rate of 10 ºC/min, in an inert nitrogen atmosphere.

In order to map the surface of CNCs/Clay thin films, it was used the profilometry characterization technique. This procedure was conducted by an AlphaStep® D-600 Stylus Profiler from KLA Tencor, using a scanning speed of 0.2 mm/s and a stylus force applied of 1 mg.

The morphology of each sample was examined by scanning electron microscopy (SEM). Two SEM images sets of CNCs/Clay thin films were acquired using two different equipment's. The first SEM images were obtained with a Carl Zeiss Auriga CrossBeam (SEMFIB) system, equipped with an Oxford energy dispersive x-ray spectrometer. The images were acquired with an acceleration voltage of 2 and 5 kV and an aperture size of 20 and 30 μm. The characterized samples were glued, with double-sided tape, to a sample holder and were subsequently coated with a mixture of gold and carbon using a Q300T D sputter coater from Quorum Technologies. The second set of SEM images were acquired by a Vega3 Tescan (Tescan, Brno, Czech Republic). Prior to examination, the samples were coated with a gold/palladium (Au/Pd) thin film, by sputtering, using the sputter coater equipment (Quorum Technologies).

In order to measure the width of the prepared films, it was used a Mitutoyo Digimatic Micrometer. Each film was measured, at least, 10 times at different positions.

Macroscopic photographs of the solid films, thin films and suspensions, were taken with a Canon 550D camera, outfitted with a Canon EF-S 60 mm Macro lens under visible light. Photographs were taken with left and right circular polarizers or crossed polarizers.

Polarized Optical Microscopy (POM) images were acquired by using and Olympus BX-51 connected to a cold light source (Olympus KL2500), coupled to a camera (Olympus DP73) and an Olympus Stream Basic 1.9 software. Using the program Lightscan 1.1.17 (mode sense +) in combination with the microscope, the spectra of reflectance of visible light of the samples were obtained.

4 Results and Discussion

The aim of this work is to develop original, environmentally friendly, nano-structured surfaces and coatings with engineered optical functionality for coloration and reflection of light. The surfaces and coatings will be fabricated from cost effective and sustainable natural materials, such as cellulose and clay.

Initially a characterization (structural and dimensional, chemical and optical) of the starting materials, used throughout the work, is presented. In which the starting cellulosic material (CMC) is compared to the isolated material (CNCs). The results of the characterization techniques (DSC-TGA, FTIR, AFM, XRD and EA) are then analyzed in detail.

Thin films (i.e. films from drop-casted method) produced via solvent evaporation of CNCs mixed with NaFh in different ratios, were studied and characterized. Different substrates (microscope slides and ITO with UVO treatment) and evaporation rates (4 ºC, 20 ºC and 60 ºC) were used to study the influence of the evaporation rate and the hydrophilic or hydrophobic effect on the thin films reflected coloration. Solid films of CNCs mixed with NaFh and Cs-Ds were produced and characterized later in this work. Both the thin films and the solid films (casted by solvent evaporation method in Petri dishes) were characterized.

4.1 CNCs characterization

First the starting material (CMC) as well as the produced material (CNCs), were chemically, structurally, morphologically and optically characterized in order to assess whether the performed acid hydrolysis reaction was successful. The FTIR, XRD and DSC-TGA analysis can be observed in Figure 4.1 (a), (b) and (c), respectively.

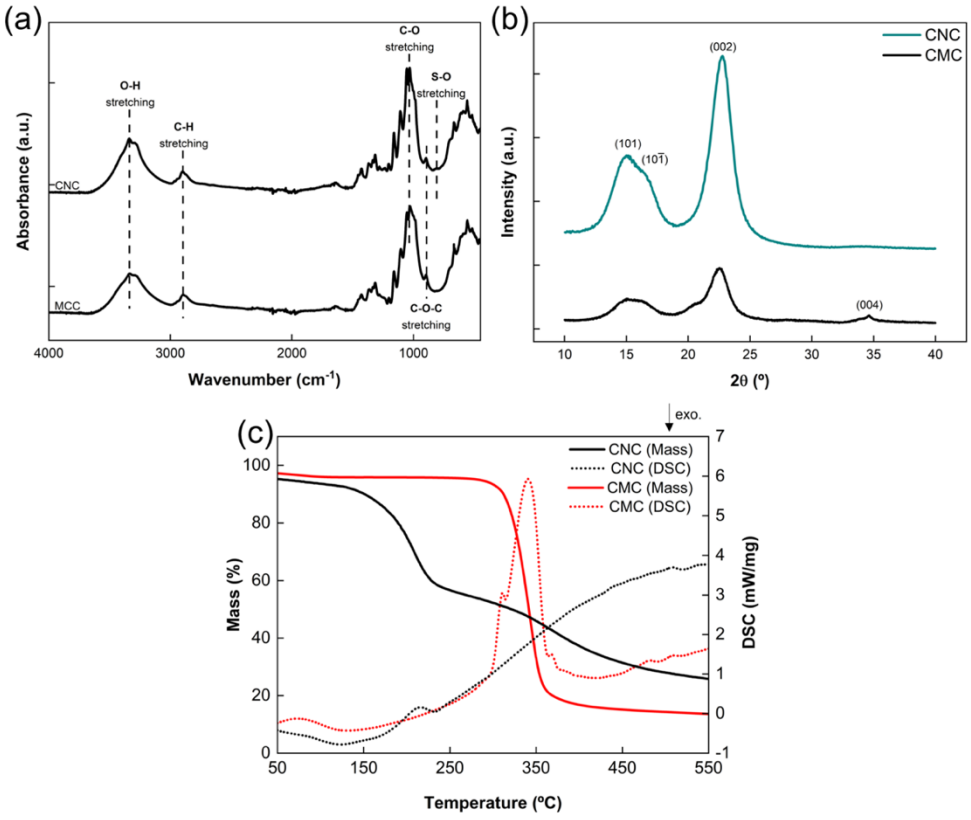

Figure 4.1 – (a) FTIR spectra of CMC and CNCs samples, submitted for analysis. (b) XRD diffractograms patterns of the synthetized CNCs (green line) and its starting material CMC (black line) samples. (c) The DSC-TGA analysis of cellulose nanocrystals (black lines) and microcrystalline cellulose (red lines).

The FTIR spectra of both samples (CMC and CNCs) that were submitted for analysis is given in Figure 4.1 (a), where the absorbance bands of the stretching vibrations are visible. Each individual vertical line represents an absorbance of stretching vibrations of the cellulose molecules. By examinating Figure 4.1 (a) it is possible to establish that both samples display the same cellulose characteristic bands at 3330, 2900 and 1030 cm^{-1}, approximately, which are in accordance with the theoretical values found in literature. These bands correspond to the stretching vibrations of O-H, C-H and C-O bonds, respectively [48]. The absorbance band at 890 cm^{-1} is associated with the stretching vibration of C-O-C bond of β(1,4) glycosidic linkage [49]. It is also possible to visualize another band at 820 cm^{-1} which corresponds to the S-O bond stretching [50]. This last one can only be observed in the spectra of the CNCs sample, it is only visible in samples, which went through an acidic hydrolysis process (in other words, that have sulfate groups present the cellulose structure). This chemical reaction can be observed in Figure 4.2.

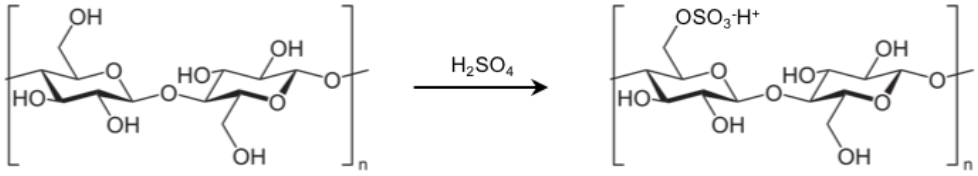

Figure 4.2 – Representation of the preparation of CNCs by acid hydrolysis of cellulose, using sulfuric acid.

The x-ray diffractograms patterns of the synthetized CNCs (green curve) and its starting material, CMC, (black curve) samples are displayed in Figure 4.1 (b). By interpreting the data, it is possible to observe the main peak at 2θ = 22.7 º which is consistent with crystalline plane 002. Two smaller peaks can be observed at 2θ = 15.0 º and 2θ = 16.6 º corresponding to the 101 and $10\bar{1}$ planes, respectively [51]. These results correspond to the characteristic peaks of cellulose type I, thus one can conclude that the cellulose structure remains stable after the acidic hydrolysis process [52]. In the diffractogram pattern of the CMC sample there is a small peak, at 2θ = 34.6 º, corresponding to the 004 plane.

Using the data from the diffractograms patterns the crystallinity index (CrI) of each characterized sample using the documented empirical method of Segal *et al* [53].

The CrI is determined by using the data extracted from Figure 4.1 (b) in combination with Equation 2:

$$CrI = \frac{(I_{(002)} - I_{am})}{I_{(002)}} \times 100 \qquad \text{Equation 2}$$

Where $I_{(002)}$ corresponds to the maximum diffraction intensity of the 002 plane, at a 2θ angle comprised between 21 º and 23 º, I_{am} corresponds to the minimum diffraction intensity of the amorphous region at a 2θ angle between 18 º and 20 º. The crystallinity index of each sample is presented in Table 1.

Table 1 – Crystallinity index of CMC and CNCs samples.

Sample	CrI (%)
CMC	75.2
CNCs	89.8

The CrI of the CNCs (89.8%) increased, in comparison to the CrI value of the CMC sample (75.2%), due to the acidic hydrolysis process in which the amorphous regions were removed. These are in accordance with the values found in the literature for a cotton source [50]. Hoeger

et al presented an identical crystalline index for CNCs from Avicel PH-101 (88%) using similar conditions (65% (w/w) sulfuric acid, 55 ºC, 30 min).

The DSC-TGA analysis of both cellulose nanocrystals (black lines) and microcrystalline cellulose (red lines) is presented in the Figure 4.1 (c). From this characterization it is possible to analyze the thermal stability of the obtained material by acidic hydrolysis (CNCs) and to compare it with its starting material (CMC).

Any mass change before 100 ºC, on both samples, occurs as a result of the evaporation of residual water, that remained in the cellulose fibers. The CMC sample shows a single sudden decline in the TGA line, between 260 ºC and 360 ˚C, as a result of a mass loss of cellulosic material and a series of degradation process of cellulose take place, such as dehydration, decomposition, and depolymerization of the glycoside units [54], [55].

The CNCs sample suffered an acidic hydrolysis process, performed with H_2SO_4, turning the degradation process in a second order pyrolysis reaction, with two mass change events. A sharp mass drop, known as the first degradation step in the CNCs sample, can be observed at temperatures between 130 ºC and 240 ºC. The direct aftereffect, to this step, is the degradation of the regions that are more accessible to sulfate groups [54], [56]. The second degradation step corresponds to the degradation breakdown of the more crystalline regions of the sample, which are less susceptible to the hydrolysis process [54]. Beyond the temperature of 400 ºC occurs the cellulose oxidation leading to the formation of carbon-based residues of the samples [55].

In Figure 4.3 is represented the Atomic Force Microscopy (AFM) image obtained for the CNCs sample, which can help in the dimensional characterization of the sample.

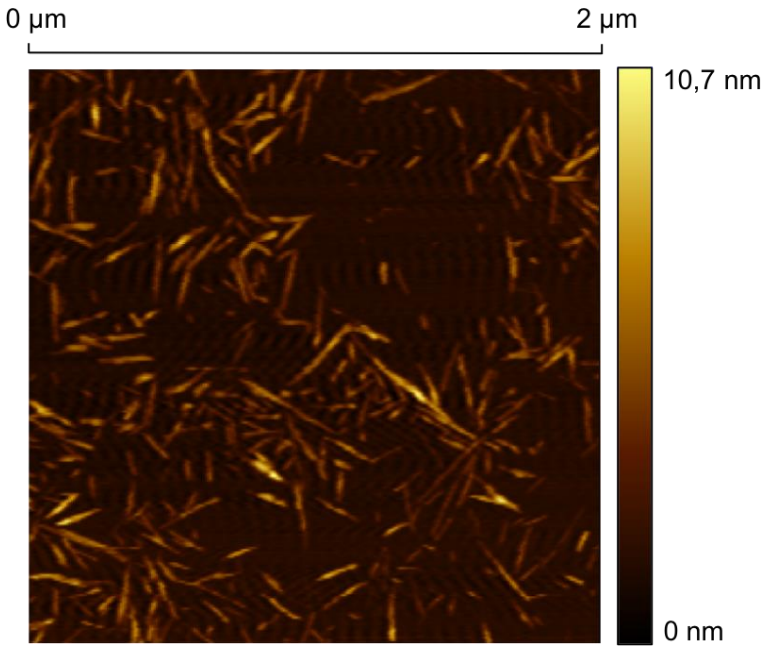

Figure 4.3 – AFM image, in amplitude retrace mode, of a diluted aqueous CNCs suspension. Window dimensions: 2 µm by 2 µm.

The acquired AFM image shows a dehydrated droplet, of the diluted, 0.01% (w/w), aqueous CNCs suspension. In order to assess the dimensions (length and width) of the “rice-like” CNCs structures, 150 measurements were made using the Gwyddion software. The mean value of the length and width measured are 182 ± 34 nm and 5 ± 1 nm, respectively, which corresponds to an aspect ratio of 36. The obtained length is within the range presented by Fernandes et al. (152 ± 65 nm) [23] and in accordance to the values listed by Rochas and co-workers for similar hydrolysis conditions (65% (w/w) sulfuric acid, 45 ºC and 30 min) [57]. The few discrepancies could be

related to the measuring method used. Additional information, such as tables and distribution graphs, regarding the AFM measurements can be found in the supporting information 7.1.

The amount of sulfate ester groups in the anhydroglucose units present in the CNCs chains can be quantified by elemental analysis (EA) characterization technique. Table 2 shows the collected data regarding the percentage of Carbon, Hydrogen and Sulfur of each sample in addition to the pure cellulose predicted values and the calculated value of the average Degree of Substitution ($\overline{DS}$) of the -OSO_3H/100 anhydroglucose units (n).

Table 2 – Percentage of each element (C, H, S and O) in the CMC and CNCs sample, obtained by elemental analysis. The Oxygen (% (w/w)) percentage was obtained by mass difference between all elements. Values obtained with an accuracy of 0.3%.

Sample	Carbon (% (w/w))	Hydrogen (% (w/w))	Sulfur (% (w/w))	Oxygen (% (w/w))	-OSO_3H/100
Pure Cellulose predicted values [58]	44.44	6.18	-	49.38	-
CMC	42.85	6.30	-	50.85	-
CNCs	38.93	6.20	0.76	54.11	3.92

By observing the data one can conclude that the CMC sample doesn't have the sulfur element present in its chain. The reason for this is that this sample wasn't submitted through the process of acidic hydrolysis with sulfuric acid.

Using the values present on Table 2 in combination with the method presented by Hamad *et al.* [59] (Equation 3), it is possible to determine the value of the Degree of Substitution of the -OSO_3H/100 anhydroglucose units (n), according to the formula $C_6H_{10}O_5$–(SO_3).

$$n = \frac{100 \times 162.141 \times S(\%)}{3206.6 - 80.063 \times S(\%)}$$ Equation 3

Where S(%) is the measured value of sulfur by elemental analysis. This sulfur content of the CNCs sample is 0.76% which is equal to the value presented by Hoeger *et al.* (0.76%) for similar hydrolysis conditions [60]. The calculated value of n of -OSO_3H/100 anhydroglucose units for the CNCs sample is calculated as 3.92 that is slightly higher than the one published by Fernandes *et al*. (4.39 -OSO_3H/100 anhydroglucose units) [23]. This discrepancy is probably due to the hydrolysis time performed by the authors, 130 min, since the longer reaction time translates into a greater degree of substitution and therefore a higher value of n.

The aqueous suspension of cellulose nanocrystals was diluted in five different concentrations, 3.03, 4.5, 5.5, 6.5 and 8.5% (w/w), in order to obtain the phase diagram (Figure 4.4). Each diluted suspension was sonicated and let to rest for 4 weeks until a visible separation was achieved. In the upper less dense isotropic phase of the nanoparticles are randomly organized while in the anisotropic lower phase, higher density, the particles are organized and a birefringence appears. The macroscopic image of phase separation, observed between crossed polarizers, is given in Figure 4.4 (a) and the corresponding volume fraction of the anisotropic phase of each suspension, obtained by dividing the height of the anisotropic phase by the total height, can be seen in Figure 4.4 (b).

A phase separation can only be observed in the samples with a concentration ranging from 3.03 to 5.5% (w/w), in which there is an isotropic (top) and anisotropic (bottom) phase separation. The two samples with a higher CNCs concentration, of 6.5 and 8.5% (w/w), only display an

anisotropic phase (see Figure 4.4 (a)). The volume fraction of the anisotropic phase for each sample as function of the CNCs concentration, shows that the anisotropic phase increases with the addition of CNCs, although this increase is not linear [61].

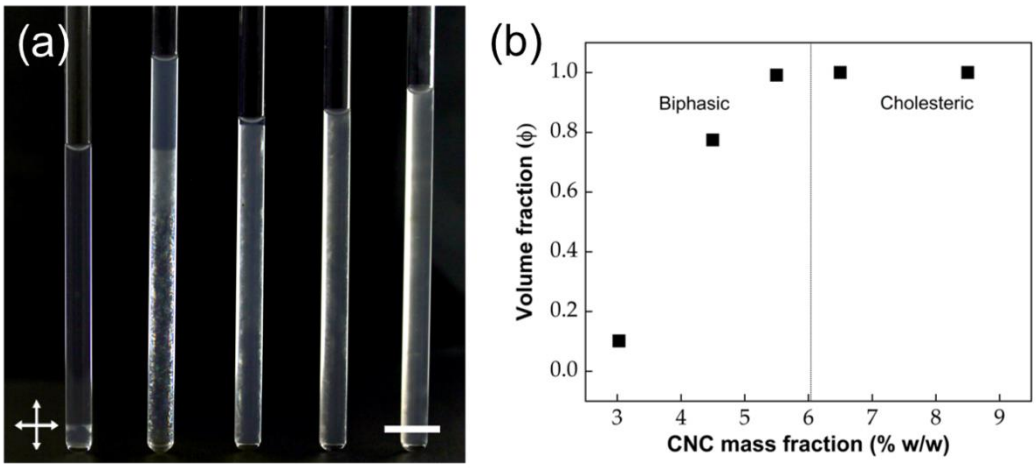

Figure 4.4 – (a) Macroscopic photograph of the phase diagram observed between crossed polarizers of CNCs suspension with a concentration, from left to right, of 3.03, 4.5, 5.5, 6.5 and 8.5% (w/w); (b) Volume fraction (ϕ) of anisotropic phase of CNCs suspension for the same suspensions. Scale bar (a) 1 cm.

Two of these suspensions of CNCs samples (with 4.5% and 8.5% (w/w)) were observed between crossed polarizers and the POM images were obtained and are presented in Figure 4.5.

In both images of the Figure 4.5, tactoids with periodically spaced birefringent bands can be seen [62]. Black regions can be observed in both samples images and correspond to the isotropic phase of the CNCs suspension. It is also observed that in the sample with a concentration of 4.5% (w/w) in CNCs (Figure 4.5. (a)) there are more black areas in comparison with the sample with 8.5% (w/w) (Figure 4.5 (b)), which leads to the conclusion that as the CNCs concentration increases there is a decrease of the isotropic regions. This conclusion is in agreement with the phase diagram of the suspensions CNCs in water, presented in Figure 4.4. It seems that the phase diagram for samples with higher concentrations of CNCs (8.5% (w/w)) is completely anisotropic at a macroscopic level, while in the microscopic pictures still exhibit a few isotropic (black) regions.

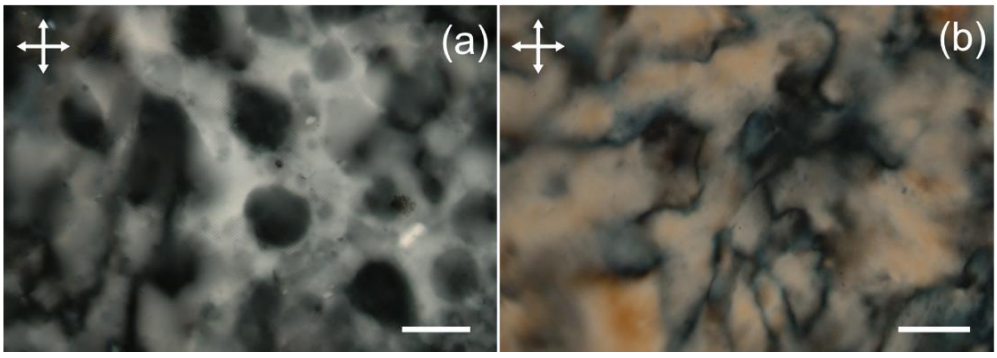

Figure 4.5 – POM images of the CNCs suspension obtained in transmission mode of (a) bi-phase (isotropic droplets in an anisotropic matrix) with 4.5% (w/w) and (b) anisotropic domain with 8.5% (w/w). Scale bar (a) 100 µm and (b) 200 µm.

4.2 CNCs/Clay thin films by drop-casting method

The CNCs suspension (2.47% (w/w)), obtained from acidic hydrolysis, was mixed with an aqueous suspension of Sodium-Fluorohectorite (1% (w/w)) to give five different percentages (99, 98, 95, 85 and 50% (w/w)) and left to rest for 5 weeks, in order to study the phase separation of the mixture of both suspensions CNCs/water and NaFh/water (i.e. CNCs/NaFh). A phase diagram of these mixtures was obtained (Figure 4.6 (a)) and the volume fraction of the anisotropic phase was calculated and plotted in Figure 4.6 (b).

The first and last vials, which corresponds to the suspensions of CNCs (i.e. 2.47% (w/w) CNCs) and pure NaFh (i.e. 1% (w/w) NaFh) in water respectively, are used as baseline for comparison between the other concentrations. At the time of the macroscopic photograph, the vial corresponding to 1% (w/w) NaFh nanoclay in water did not present a visible phase separation.

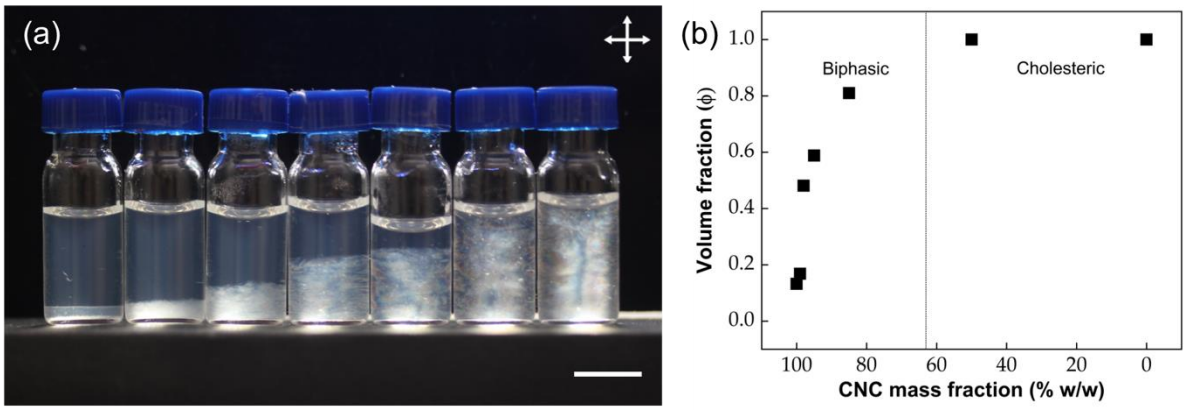

Figure 4.6 – (a) Phase diagram observed between crossed polarizers of the CNCs suspension (2.47% (w/w), CNCs/NaFh mix suspension (with 99, 98, 95, 85 and 50% (w/w) of CNCs) and NaFh suspension (1% (w/w) in water), respectively; (b) Volume fraction (ϕ) of anisotropic phase for the same suspensions. Scale bar (a) 1 cm.

The vials with a CNCs percentage ranging between 99 and 85% (w/w), showed a visible phase separation while the mixture of 50% (w/w) of CNCs and the NaFh suspension (1% (w/w) in water) exhibited only a single anisotropic phase. The anisotropic phase increases with the nanoclay NaFh percentage in the suspension. In Figure 4.6 (b) it can be observed that the amount of clay has a big influence on the volume fraction since anisotropic phase increases 34.9% by adding only 2% (w/w) of nanoclay.

Using these aqueous suspensions, an initial test was performed thru preparing thin films by drop-casting method, from the suspension with 98% CNCs / 2% NaFh (w/w). The test was conducted with a variable substrate and temperature of evaporation (Figure 4.7) with the purpose of assessing the optimal conditions in which the coloration of the samples display the best features. By observing the POM images one can state that the samples reflect all LCP light and transmit all RCP light.

Comparing the POM images, regarding the samples with different evaporation temperatures, the samples that show the best reflected coloration within the visible spectrum are the ones evaporated at 4 ºC (Figure 4.7 (a) and (d)). These samples display a lower spectral width in the LCP light channel, which corresponds to a more defined reflected coloration in comparison with the other temperatures (20 ºC and 60 ºC). The spectral width of a LCP reflected spectrum corresponds to the Full Width at Half Maximum (FWHM) of the maximum wavelength peak. The samples with higher evaporation temperatures (20 ºC: Figure 4.7 (b), (c) and 60 ºC: Figure 4.7 (e), (f)) show a larger spectral width and a section of the reflected spectra of the LCP light channel is in the UV wavelength.

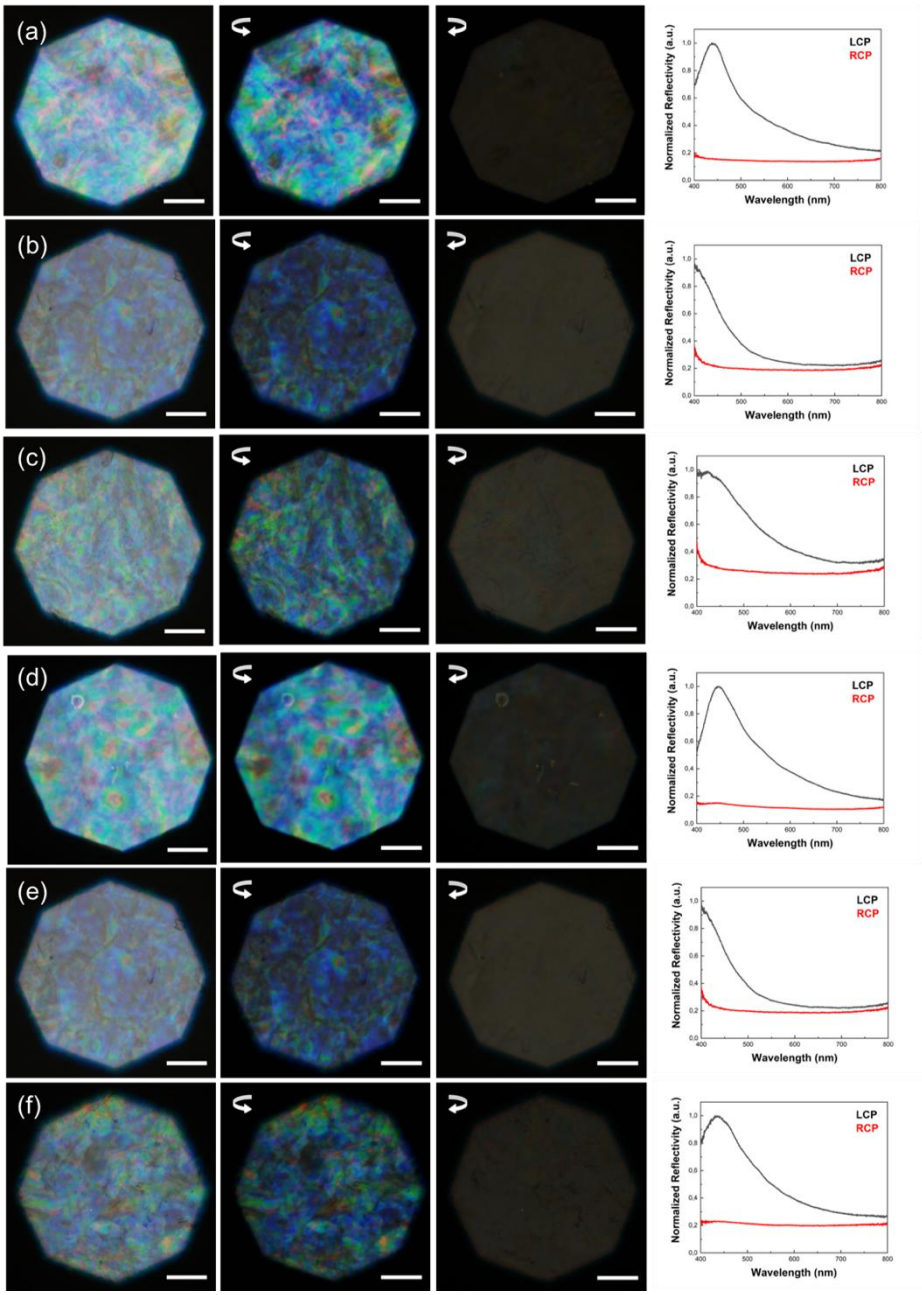

Figure 4.7 – POM images of 98% CNCs / 2% Clay (w/w) mixture from the center of the thin films, obtained in reflection mode, in conjunction with their reflectivity spectra. Thin films from (a) to (c) were dropped on ITO substrates with UVO treatment and temperatures ranging from 4 ºC, 20 ºC and 60 ºC, respectively. Thin films from (d) to (f) were dropped on microscope slides using the same temperatures, respectively. They were observed under left and right circularly polarized light. Scale bar (a) – (f) 50 µm.

A sample with a homogenous coloration across the surface is more desirable in comparison with a heterogeneous coloration. Therefore, it is essential to assess which substrate provides the most homogenous coloration. Knowing this, two deposition substrates were studied, ITO coated glass with UVO treatment (Figure 4.7 (a) to (c)) and microscope slides (Figure 4.7 (d) to (f)). The main difference between these two substrates is their hydrophilicity, in other words the way in which the droplet interacts with the surface of the substrate. The microscope slides are made out of glass, so they are naturally prone to be highly hydrophobic, which means that the thin film in this substrate will have a superior thickness. The ITO coated glass substrate is also hydrophobic, therefore it was submitted to a UVO treatment in order to become hydrophilic in the area treated, as explained below.

The UVO treatment consists in the intense emission of two ultraviolet wavelengths, 185 nm and 254 nm. The 185 nm wavelength will dissociate the molecular oxygen (O_2), present in the air, creating atomic oxygen and then the atomic oxygen will react with molecular oxygen and create Ozone (O_3). When O_3 is irradiated with 254 nm UV light, it decomposes [63]. Due to the surface oxidation, caused by UVO treatment, the wetting properties change, leading to an increase of the surface hydrophilicity. This treatment has a time limit, that is to say that as time elapses the treated area becomes less hydrophilic.

Once a droplet is drop-casted onto this surface, it will spread across the treated area, while at the same time restrained by the hydrophobic surrounding area, leading to a thinner and homogenous deposition. Since the thickness of the evaporated droplet is interconnected to the pitch of the cholesteric structure (directly proportional) it is of great interest to reduce its thickness in order to obtain a more homogenous thin film.

In addition to POM images and reflectivity spectra, the surfaces of the samples were scanned by a profilometer, whose graphs are represented at Figure 4.8, in order to observe the influence of the different evaporation rates on the surface of the thin film and verify the existence of the "coffee stain" effect. Analyzing the scans of the samples, the "coffee stain" effect is observable in the thin films produced at higher evaporation temperatures (20 ºC and 60 ºC).

The "coffee stain" effect occurs when the particles migrate to the outer edge (contact line) of the droplet, leaving a ring-like deposit [57]. The pinned contact line makes the particles flow to the edges (visible in the schematic representation in Figure 4.9), due to differential evaporation rates across the droplet (the evaporation rate is higher at the extremities in comparison to the center of the droplet) [64], [65].

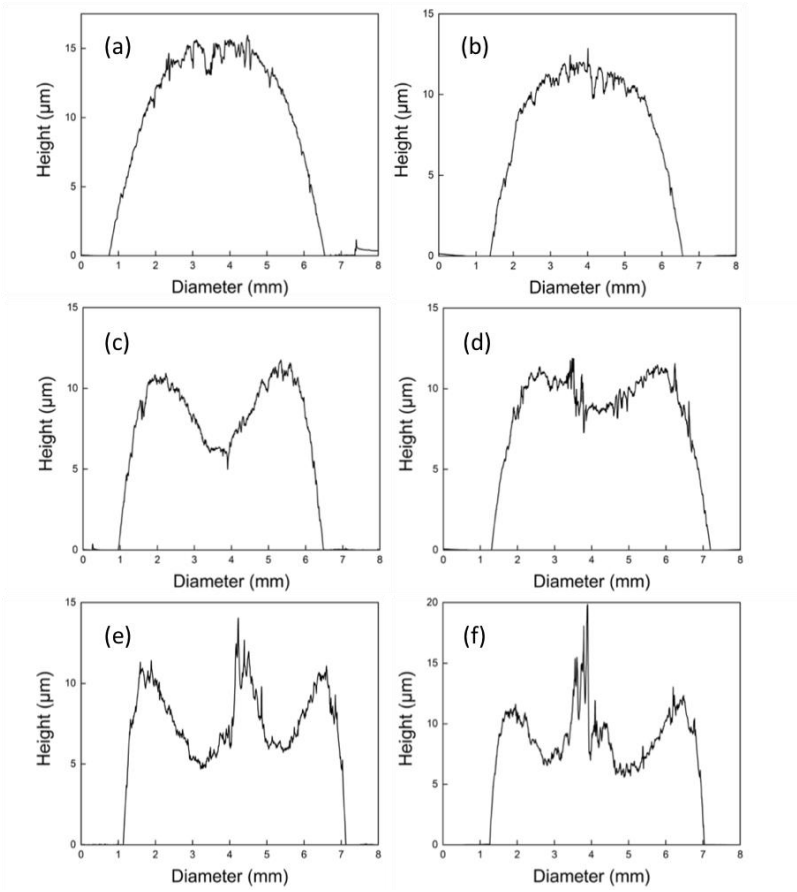

Figure 4.8 – Profilometer scan across the diameter of thin films with 98% CNCs / 2% NaFh (w/w). Samples (a), (c) and (e) were casted on microscope slides and temperatures ranging from 4 ºC, 20 ºC and 60 ºC, respectively. Samples (b), (d) and (f) were casted on ITO with UVO treatment and temperatures ranging from 4 ºC, 20 ºC and 60 ºC, respectively.

Therefore, the thickness of the thin film arises from the evaporated droplet and will fluctuate throughout the surface (i.e. though the radios of the thin film) leading to changes in the chiral nematic pitch and, so, in the coloration.

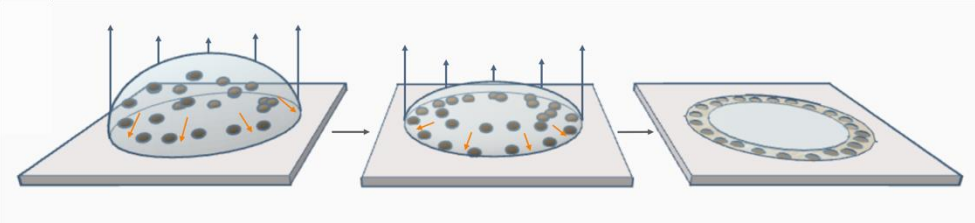

Figure 4.9 – Scheme showing the evaporation process of a droplet and formation of the “coffee stain” effect.

A lower evaporation temperature will assuredly originate a slower evaporation rate and will lead to a more uniform evaporation of the droplet. As a result, the particles in suspension have more time to get organized, which results in a homogeneous cholesteric structure organization throughout the film and the decreasing of the “coffee stain” effect.

The droplets evaporated at a slower rate, 4 ºC, (Figure 4.8 (a) and (b)) don’t show any signs of “coffee stain” effect, since a round shape along the diameter of the film is visible. Contrarily the scans from the two other evaporation temperatures, 20 ºC and 60 ºC, (Figure 4.8 (c) and (d); (e) and (f), respectively), show a concave shape characteristic of the “coffee stain” effect. In the profilometry scan corresponding to 60 ºC, this effect is furthermore noticeable since there is a substantial difference in heights of the center and the edge, confirming an intensification of particles in the outer edge of the thin film. In Figure 4.8 (e) and (f) it is possible to identify a non-uniformity (i.e. a peak) at the center of the thin films profilometer scan. This phenomenon is not usual in samples containing only cellulose nanocrystals, therefore the appearance of this peak must be linked to the added nanoclay. A possible explanation can be related to the clays tendency to swell in water [39], which implies that a significant percentage of the water present in the droplet can be trapped by the clay particles. This swelling affects the mobility of the particles to the periphery of the sample playing a crucial effect on the evaporation processes of the droplet, by capturing some of the particles at the center of the thin film.

It is noticeable that the thin films that were casted onto the treated ITO substrate exhibit a lessened “coffee stain” effect, in comparison to the ones casted onto microscope slides. With this in mind, the chosen evaporation condition in order to obtain films with uniform and defined color within the visible spectrum are 4 ºC for temperature evaporation and ITO coated glass substrate with UVO treatment.

In order to understand the color evolution, throughout the thin film, in function of the temperature, another study was developed using the same concentration (98% CNCs / 2% NaFh (w/w)) and substrate (ITO with UVO treatment). POM images of these results are shown in Figure 4.10.

Acknowledging the “coffee strain” effect (although sometimes subtle) in the thin films, the intention is to study the coloration evolution within the film, by maintaining the same substrate (ITO with UVO treatment) and concentration (98% CNCs / 2% NaFh (w/w)) and varying the evaporation temperature (4 ºC and 20 ºC). Figure 4.10 presents the POM images of this study with a 4 ºC evaporation temperature from (a) to (c) and 20 ºC from (d) to (f). In the test early performed, the center of the optical variation of thin film was characterized, but in this test the objective is to assess the effect of the temperature along three areas of the thin film: center (a) and (d), intermediary area (b) and (e), and outer edge (c) and (f). All films reflected left circularly polarized light and transmitted right circularly polarized light.

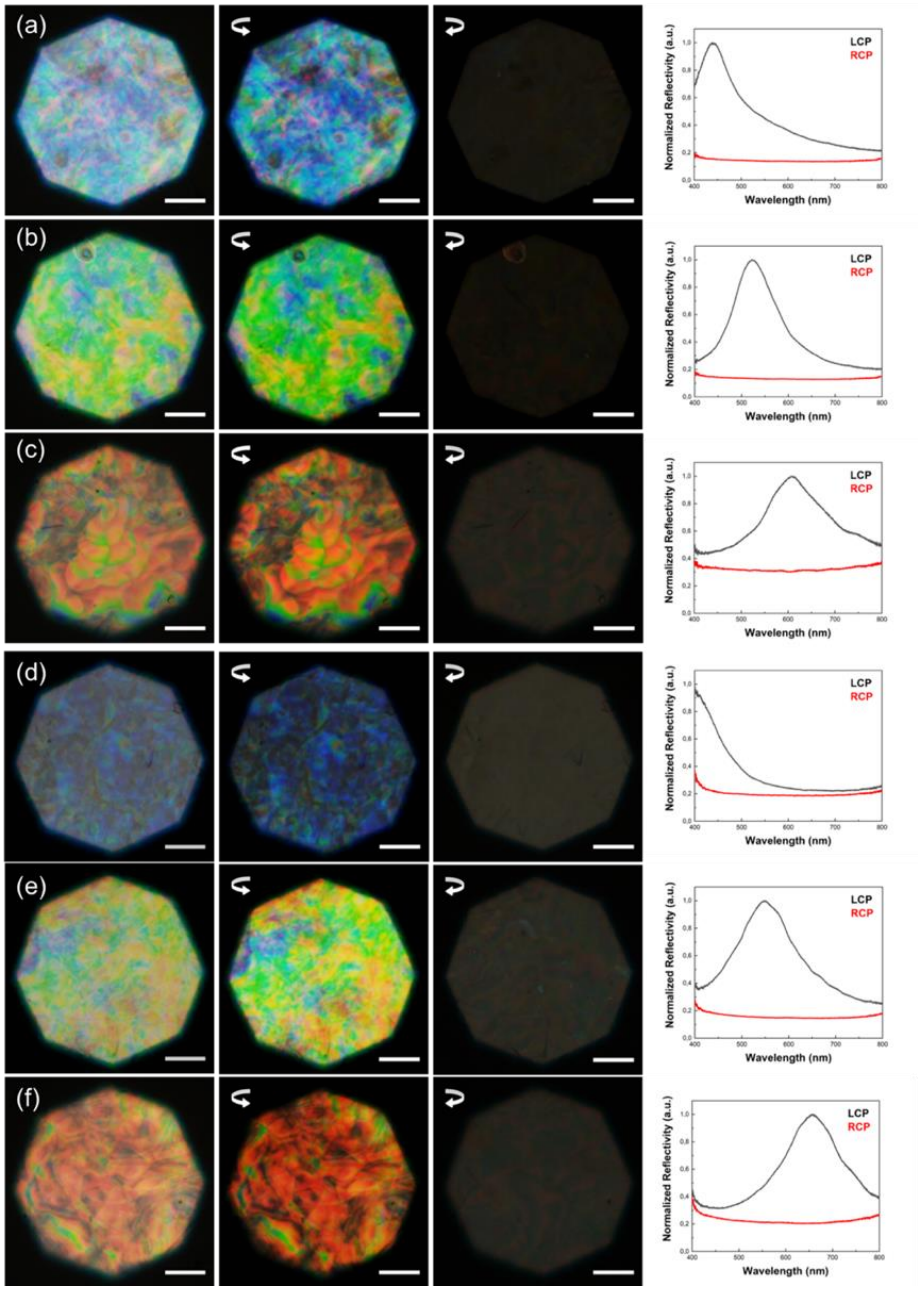

Figure 4.10 – POM images (obtained in reflection mode) of thin films with 98% CNCs / 2% NaFh (w/w) drop-casted onto a ITO substrate with UVO treatment, in conjunction with their reflectivity spectra. The evaporation temperature was 4 ºC from (a) to (c), from the center to the edge of the sample, respectively, and 20 ºC from (d) to (f) of the center, intermediate area and outer edge, respectively. The thin films were observed under left and right circularly polarized light. Scale bar (a) – (f) 50 µm.

The center of the thin film for both temperatures display a blue reflected coloration, however the sample (a), for 4 ºC, displays a brighter coloration in comparison to the sample (d), 20 ºC. This last thin film has the reflectivity spectrum partially out of the visible range, towards the UV wavelength, with a maximum below 400 nm. The intermediary area of the thin film at 4 ºC, Figure 4.10 (b), displays mostly a green reflected wavelength, with a maximum of 521nm, while Figure 4.10 (e), which corresponds to the temperature of 20 ºC, reflected coloration corresponds to both green and red, with a maximum wavelength of 550 nm. The reflected wavelength of the outer edge of the thin film, evaporated at 20 ºC (Figure 4.10 (f)), is mostly red, with a maximum of 659 nm, and the one evaporated at 4 ºC (Figure 4.10 (c)) reflects both red and green wavelengths, which can be confirmed by the width of the reflectivity spectra (197 nm) and a maximum of 608 nm.

The left circularly polarized light reflected spectral widths ($\Delta\lambda$) and maximum wavelength (λ_{max}) reflected peak of the thin films calculated from Figure 4.10 are summarized in Figure 4.11.

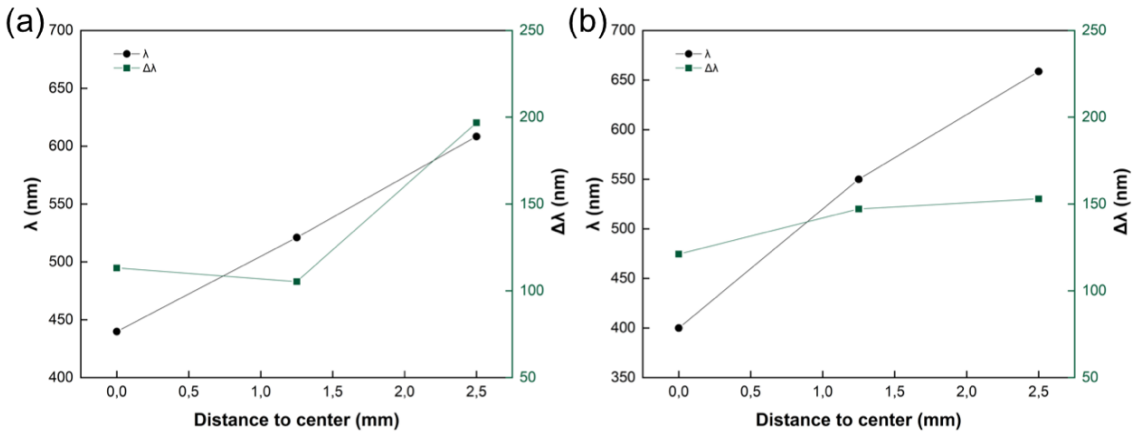

Figure 4.11 – Reflected spectral widths and maximum wavelength reflected corresponding to the center, intermediary area and outer edge of the thin films (98% CNCs / 2% NaFh (w/w); substrate: ITO with UVO treatment. The evaporation temperatures are 4 ºC (a) and 20 ºC (b).

By observing the values of the spectral widths, it seems that the evaporation rate of the droplets has an influence in the spectra reflected wavelength. A higher spectral width value means that a less specific color is being reflected by the LCP light channel, on the other hand a lower value corresponds to a more specific reflected coloration. The center, intermediary area and outer edge of the thin film correspond to 0 mm, 1.25 mm and 2.5 mm of distance to the center, respectively. The center and intermediary area of (a) show a lower spectral width in comparison with the corresponding area in (b), thus a more specific color is reflected. The outer edge of the thin film in (a) has a higher spectral width in comparison with (b), because it still reflects green and red wavelengths. Therefore, the sample (a) was less affected by the “coffee stain” effect.

The values of maximum wavelength reflected for sample (a) are overall lower in comparison with the values of sample (b). A possible justification for this variation is that the sample (a) had an evaporation temperature lower than sample (b), thus it was less affected by the “coffee stain” effect, which is in accordance with the results shown in Figure 4.8.

Using the optimal parameters of evaporation (temperature and substrate type), an assortment of droplets was drop-casted in order to analyze the effect of mixing CNCs with NaFh. The suspensions selected were 100% (w/w) CNCs, 99% CNCs / 1% NaFh (w/w), 98% CNCs / 2% NaFh (w/w), 95% CNCs / 5% NaFh (w/w), 85% CNCs / 15% NaFh (w/w) and 50% CNCs / 50% NaFh (w/w). Macroscopic photographs of some of the thin films, produced by solvent evaporation, observed under left and right circularly polarized light can be found in Figure 4.12. All samples reflect LCP light and transmit RCP light. Indicating that CNCs cholesteric phase is ruling the handedness of the system.

The first set of photographs, (a), correspond to pure cellulose nanocrystals and show an iridescent blue coloration in the majority of the thin film and green coloration in the outer edge. The second (b) and third (c) sets of photographs were taken from thin films with 1 and 2% (w/w) of NaFh added, respectively. These two sets show a green shift of the reflected coloration.

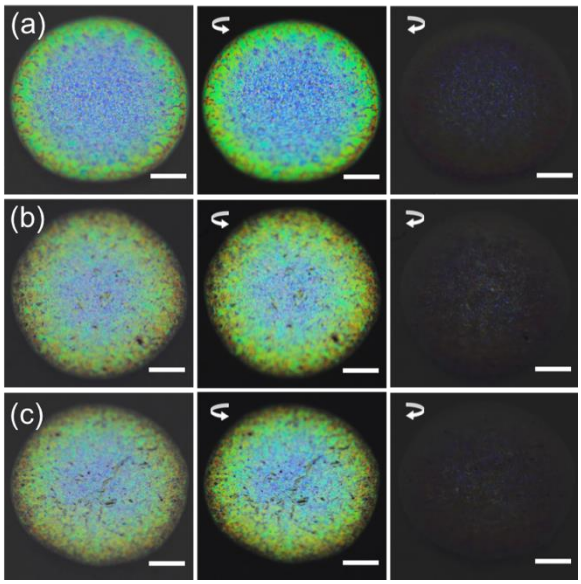

Figure 4.12 – Macroscopic photographs of thin films from CNCs and NaFh. The thin films were observed under visible light, left and right circularly polarized light. Scale bar (a) – (c) 7.5 mm.

POM images in transmission mode, under crossed polarizers, of the thin films with CNCs and NaFh, that presented coloration, are shown in Figure 4.13, where patterned fingerprint textures can be observed. Previously in this work aqueous suspensions of CNCs showed tactoids, which are well organized chiral nematic structures [27], when observed by POM in transmission mode, even for concentrations with only anisotropic phase (Figure 4.5). These tactoids tend to fuse to each other and become bigger due to a coalescence mechanism [62]. When the water of the CNCs/NaFh films is allowed to evaporate, the tactoids organization is retained and ultimately become part of the fingerprint texture [62]. Therefore one can state that the cholesteric order was not disrupted [45]. These patterns are observed when the tactoids orientate perpendicularly to the point of view of the viewer.

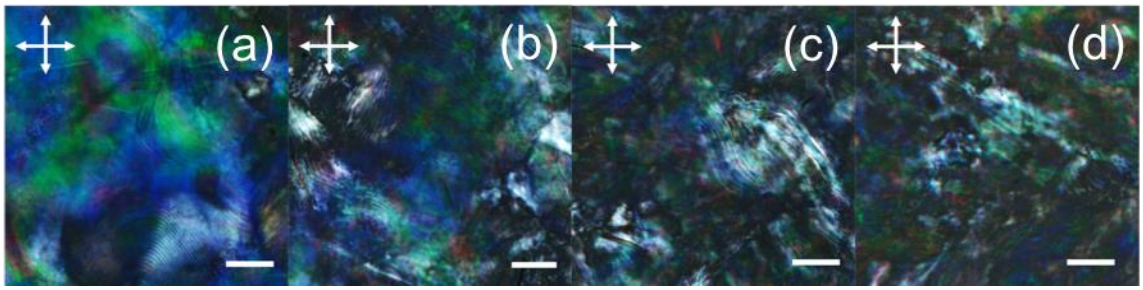

Figure 4.13 – POM images of CNCs/NaFh thin films texture, observed in transmission under crossed polarizers. (a) 99% CNCs / 1% NaFh (w/w), (b) 98% CNCs / 2% NaFh (w/w), (c) 95% CNCs / 5% NaFh (w/w) and (d) 85% CNCs / 15% NaFh (w/w) Scale bar 20 µm.

The POM images in conjunction with the wavelength spectra, of the thin films from the mixtures, are visible in Figure 4.14. By observing the images one can see that most of the samples reflect all left circularly polarized light and almost none right circularly polarized light.

The first thin films, Figure 4.14 (a), containing 100% (w/w) CNCs, display an almost homogenous blue reflected visible light. In comparison the samples, with 1 and 2% (w/w) NaFh (Figure 4.14 (b) and (c)), display a slight less homogenous blue reflected light in the LCP channel, consequently showing a wider LCP reflectivity spectra and a lower wavelength. In Figure 4.14 (d), 5% (w/w) NaFh, one can state that the reflected wavelength is higher and a green reflected visible light is observable in the POM images.

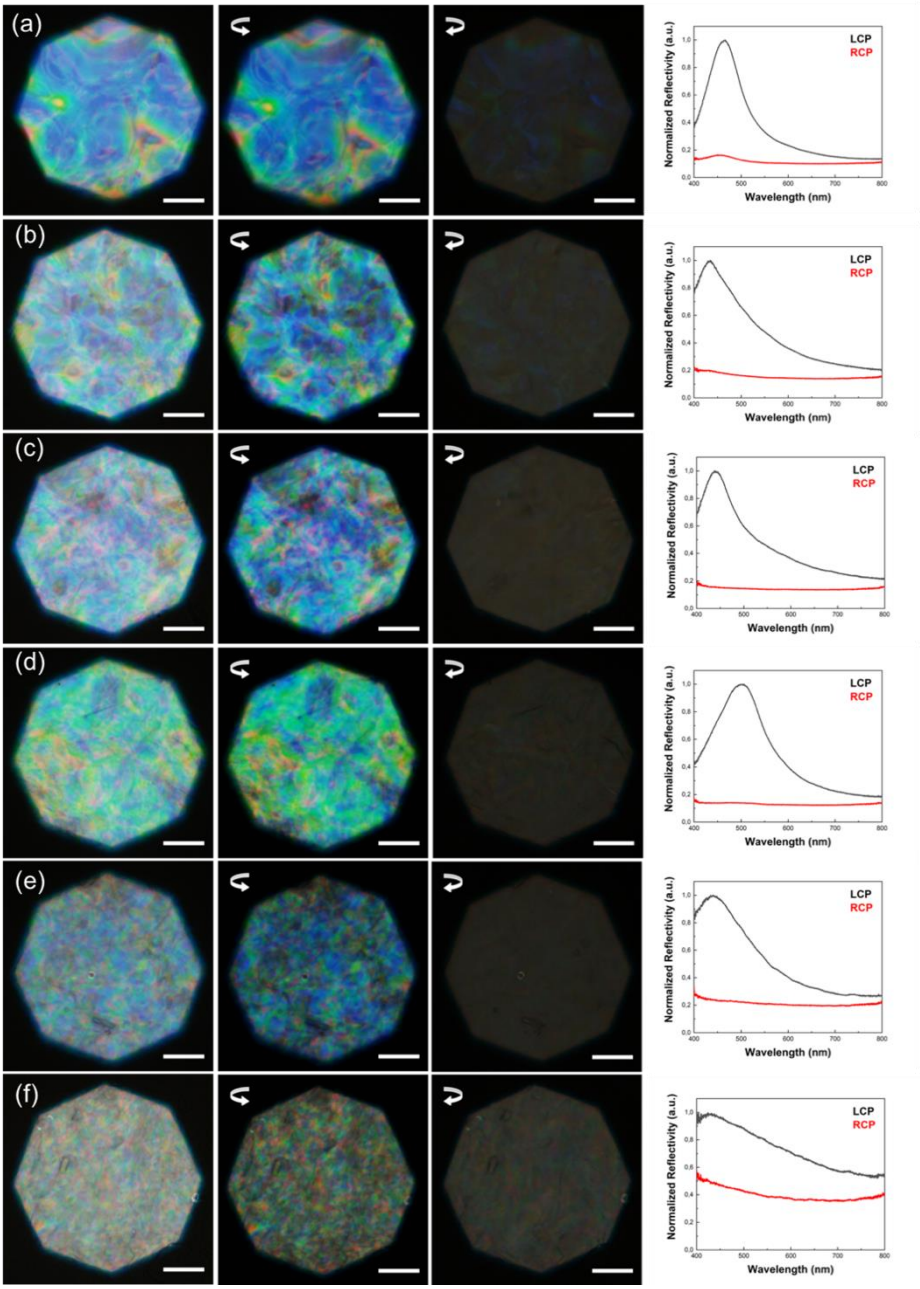

Figure 4.14 – POM images of CNCs/Clay mixtures thin films center (temperature: 4 ºC; substrate: ITO with UVO treatment), obtained in reflection mode, in conjunction with their reflectivity spectra. The percentage of NaFh in each thin film is (a) 0, (b) 1, (c) 2, (d) 5, (e) 15 and (f) 50% (w/w). The thin films were observed under left and right circularly polarized light. Scale bar (a) – (f) 50 µm.

The sample with 15% (w/w) NaFh (Figure 4.14 (e)), displays a visible regression of the reflected spectrum, showing blue and green reflected light in the LCP channel and at the same time a larger spectral width. The last thin film (Figure 4.14 (f)), with 50% (w/w) NaFh, loses coloring, starts to reflect RCP light and the reflected LCP light no longer has a defined and homogenous coloration. Inspecting the reflectivity spectrum it is visible that the peak wavelength, of the LCP channel, is much wider and the RCP channel reflects visible light.

Taking in account the previous data, one can clearly state that it is possible to obtain thin films with iridescent coloration by mixing CNCs and nanoclay NaFh and achieve different colors by varying the ratio of CNCs/NaFh.

From the spectra in Figure 4.14, referring to the reflectivity spectra, it is possible to determine the maximum wavelength peak and spectral width. Using the *de Vries* equation, (Equation 1), mentioned earlier in this work, assuming $\theta = \frac{\pi}{2}$, it is possible to calculate the pitch value of the samples, by dividing the wavelength peak by the refractive index of CNCs (1.56), assuming that this value was not affected by the low quantity of added clay. These values are displayed in Table 3. The data shows that by adding 5% (w/w) of NaFh the maximum wavelength peak increases, therefore a green shift is reported. The sample with 15% (w/w) of NaFh has a spectral width significantly bigger than the others, since this sample's clay percentages is near the critical quantity of NaFh added that can still obtain coloration. As already seen earlier the sample with 50% (w/w) of CNCs has the biggest spectral width (292 nm) when compared to other thin films, since its coloration faded.

Table 3 – Maximum wavelength peak (λ_{max}), spectral width ($\Delta\lambda$) and pitch value of the thin films prepared, from various CNCs/NaFh ratios.

[CNCs] (% (w/w))	**Maximum Wavelength, λ_{max} (nm)**	**Spectral width, $\Delta\lambda$ (nm)**	**Pitch (nm)**
100	466	81	299
99	435	149	279
98	440	110	282
95	506	127	324
85	436	195	279
50	420	292	269

SEM images of the thin films cross-section were acquired, Figure 4.15. By observing the CNCs sample (Figure 4.15 (a)) one can conclude that it possess a chiral nematic structure while the NaFh sample (Figure 4.15 (b)) shows a lamellar structure, according to literature [64], [66].

In Figure 4.15 (c) and (d) the SEM images show the morphology of cellulose nanocrystals mixed with nanoclay with two different percentages (58% NaFh / 42% CNCs (w/w) and 5% NaFh / 95% CNCs (w/w), respectively). The sample, with a higher percentage of CNCs, Figure 4.15 (d), displays a helicoidal orientation, derived from the chiral nematic suspension, even if there is a small quantity of nanoclay present in the suspension. Thus, there is a strong possibility that by mixing these materials, in specific quantities, one can obtain colored films since the helicoidal structure is not lost due to the presence of the clays.

Figure 4.15 (c) shows the cross-section of the sample with a greater percentage of NaFh and in this thin film a lamellar structure is present. Hence there is a maximum percentage of nanoclay that can be mixed with cellulose nanocrystals in order to obtain colored thin films. The addition of CNCs can add to the clays lamellar structures a chiral left-handed structure. The SEM images indicate that by mixing CNCs with the NaFh clay the cholesteric arrangement of the CNCs can be preserved in the solid state, which translates into the coloration observed in the thin films prepared.

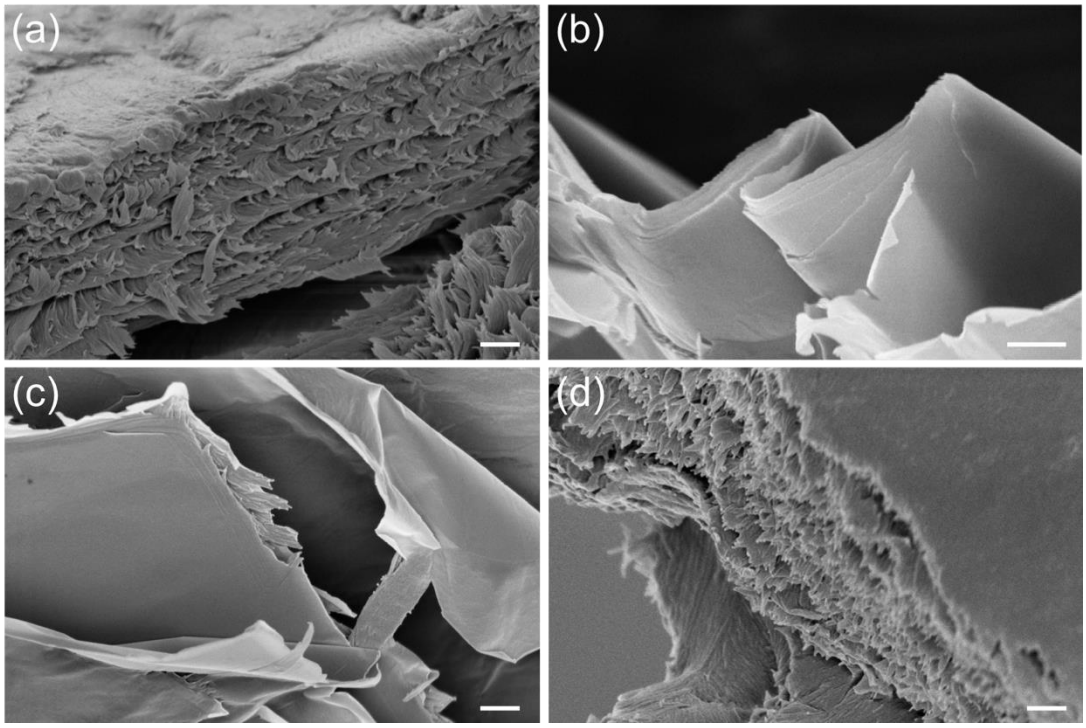

Figure 4.15 – Cross-section SEM images of thin films from (a) 100% (w/w) CNCs; (b) 100% (w/w) NaFh; (c) 58% NaFh / 42% CNCs (w/w); (d) 5% NaFh / 95% CNCs (w/w). Scale bar (a) – (d) 400 nm.

In addition to the studies already described, two other were performed in order to further investigate the optical behavior that results from the interaction of the CNCs and sodium-fluoro-hectorite. The first study consisted in stacking thin films, alternating between CNCs and NaFh, creating a series of layers with different number of layers. Droplets, of 2.47% (w/w) of CNCs in water and 1% (w/w) NaFh in water, were drop-casted on microscope slides and the solution was allowed to evaporate at a temperature of 4 ºC. In Figure 4.16 a schematic representation and macroscopic photographs of the thin films produced are shown. In the schematic representation (Figure 4.16 (c)) the starting layer deposited was made from CNCs (after solvent evaporation), a droplet of nanoclay was drop-casted on the top of the CNCs thin film, and so on.

The first stacking contains one layer of CNCs and one layer of NaFh (Figure 4.16 (a)). By observing the corresponding macroscopic photograph one can see an iridescent blue coloration across the thin film. The second stacking, contains another layer of CNCs on top of the two other layers (Figure 4.16 (b)), where it is possible to observe a blue and green reflected colorations. Every added layer increased the thickness of the resulting stacking and the pitch shifted to a higher reflected wavelength. The NaFh should be transparent and in some extend the NaFh solution must diffuse through the CNCs thin film.

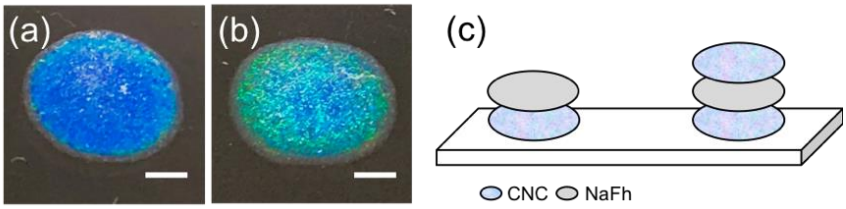

Figure 4.16 – Macroscopic photographs of thin film layer composition from CNCs and NaFh, (a) and (b), alongside with the schematic representation of the droplet order deposition, (c). Scale for (a) and (b) is 2.5 mm.

The second study consisted in drop-casting droplets, of the isotropic and anisotropic phase of pure CNCs and CNCs mixed with NaFh in various percentages. The droplets were drop-casted onto an ITO coated glass with UVO treatment substrate and evaporated at a temperature of 4 ºC. The macroscopic images of the produced thin films are shown in Figure 4.17.

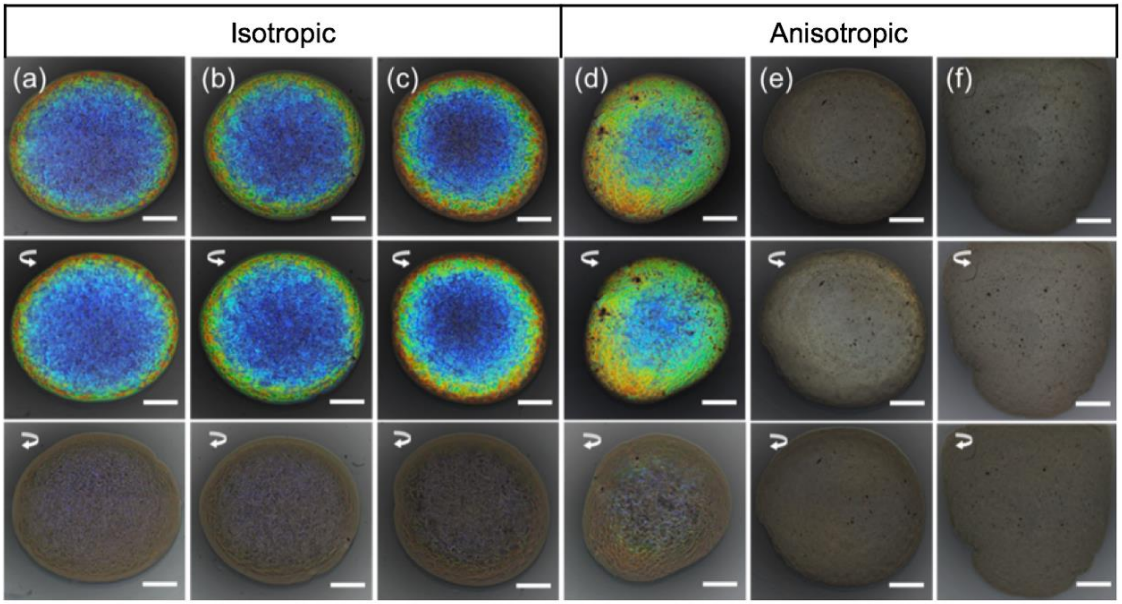

Figure 4.17 – Macroscopic photographs of thin films from the isotropic (a) – (c) and anisotropic (d) – (f) phase of pure CNCs and CNCs/NaFh suspensions. The thin films were observed under left and right circularly polarized light. Scale bar (a) – (f) 7.5 mm.

The thin films, in Figure 4.17 were deposited from drop-casted method and observed under left and right circular polarizers. Images (a) to (c) correspond to the ones deposited from the isotropic phase and the images (d) to (f) from the anisotropic phase, with the following concentrations: (a) and (d) 100% (w/w) CNCs; (b) and (e) 99% CNCs / 1% NaFh (w/w); (c) and (f) 98% CNCs / 2% NaFh (w/w).

By observing the photographs of the thin films obtained from the isotropic phase, Figure 4.17 (a) to (c), it is visible that as the nanoclay percentage increased the reflected coloration evolutions is observed as the blue center area tends to reduce while the green and red tend to rise. The intermediary area of the thin film shifted from blue to green, with the addition of NaFh, and the outer edge shifted from green and red to only a red bright coloration.

The images of the anisotropic phase, Figure 4.17 (d) to (f), show that the thin film obtained from the CNCs solution show reflected coloration on LCP light channel while the two other thin films that contain NaFh don't display any reflected coloration on the LCP light channel. This is an indication that the clay nano particles align the CNCs cholesteric pseudo layers parallel to the substrates.

The absence of coloration in the anisotropic phase is not usual in suspensions with pure cellulose nanocrystals only, therefore the added clay may be responsible for this phenomenon. Since the nanoclay particles are heavier in comparison with the CNCs particles, the percentage of NaFh in the anisotropic phase is going to be higher in comparison to the percentage of CNCs. On the other hand, since the CNCs particles are lighter the isotropic phase has bigger percentage of CNCs, therefore it has an iridescent coloration. As previously stated in this work, there is a critical concentration of CNCs mixed with NaFh needed to maintain a chiral nematic structure, but since the anisotropic phase has not met this critical concentration no coloration is going to appear in these thin films.

4.3 CNCs/Clay solid films

Using the aqueous suspensions of CNCs, CNCs mixed with NaFh and CNCs mixed with Cs-Ds, three solid films were casted by solvent evaporation method in Petri dishes (35 mm diameter). In Table 4 the concentration of CNCs in each sample, volume of suspension used and thickness obtained for each solid film are displayed. Additional information, regarding the thickness measurements, can be found in the supporting information 7.2.

Table 4 – Concentration, volume and thickness of solid films prepared, from CNCs, CNCs/NaFh and CNCs/Cs-Ds.

Sample	[CNCs] (% (w/w))	Volume (ml)	Film thickness (μm)
CNCs	100	2	26 ± 4
CNCs/NaFh	98	2	33 ± 5
CNCs/Cs-Ds	98	2	23 ± 7

These films were produced using the same amount (2 ml) of each aqueous suspension and an evaporation temperature of 4 ºC. The thickness value of the solid film from CNCs/NaFh (33 ± 5 μm), although within the error, is higher in comparison with the pure CNCs (26 ± 4 μm). This increase in thickness may be correlated to the fact that the mixed nanoclay contains bigger particles in comparison with the CNCs particles. In contrast the film of CNCs mixed with Cs-Ds, although within the error, shows a lower thickness (23 ± 7 μm) in comparison with the solid film of pure CNCs. For a better understanding the schematic representation of the organization of the nanoclay platelets are displayed in Figure 4.18.

The platelets of the Cs-Ds nanoclay are heavier in comparison with the monolayer NaFh, thus they force the helicoidal structure to have a smaller helical pitch. It is possible that the nanoclay NaFh, Figure 4.18 (a), has double the material between the platelets in comparison with Cs-Ds, Figure 4.18 (b). This means that for each group of NaFh platelets (Figure 4.18 (a)), holding the CNCs between them, only half will be present in the Cs-Ds interplatelet spaces, since they contain cesium in the other half, as already displayed in Figure 2.7.

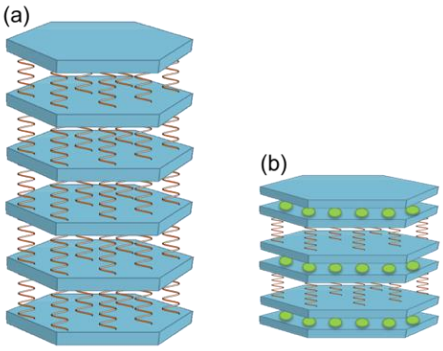

Figure 4.18 – Schematic representation of organization of the nanoclay platelets corresponding to NaFh (a) and Cs-Ds (b).

The macroscopic photographs of the three produced solid films, observed under left circularly polarized light and right circularly polarized light, are represented in Figure 4.19.

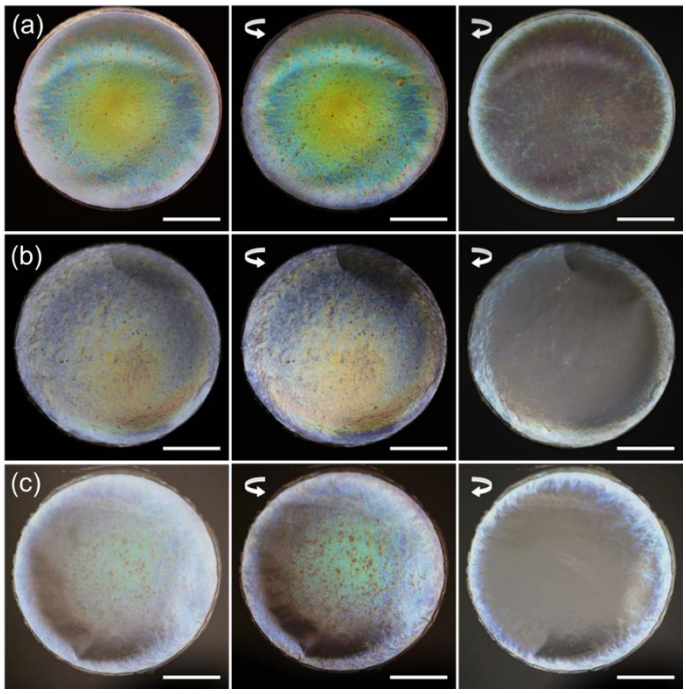

Figure 4.19 – Macroscopic photographic images of solid films from (a) 100% (w/w) CNCs; (b) 98% CNCs / 2% NaFh (w/w); (c) 98% CNCs / 2% Cs-Ds (w/w). The films were observed under left and right circularly polarized light. Scale bar (a) – (c) 1 cm.

From the photographic images, Figure 4.19, it is observable that all the solid films display an iridescent coloration. The solid films reflected left circularly polarized light and transmit almost all right circularly polarized light (only a small portion of the outer edge of the films reflect RCP light). Even though the solvent has evaporated using a slow evaporation rate, the films display a color gradient, since a reflected coloration change can be seen throughout the film.

The center of the pure CNCs film (Figure 4.19 (a)), displays an iridescent green/yellow coloration and the outer edge of the film shows an iridescent blue coloration. By adding 2% (w/w) of NaFh (Figure 4.19 (b)) a shift in the reflected coloration appears when comparing it to the pure CNCs sample (i.e. the wavelength increases). This sample displays an iridescent red coloration at the center and blue at the outer edged of the film. The reason behind the increase of the reflected wavelength may be attributed to the increase of the thickness of the film, that was described previously. The center of the solid film with 2% (w/w) of Cs-Ds mixed with 98% (w/w) of CNCs (Figure 4.19 (c)), reflects a green iridescent coloration that leads to a blue coloration at the edge.

These films were also observed by POM, working in the reflection mode, and the resulting images are shown in Figure 4.20. They were observed under left and right circularly polarized light and their reflectivity spectra were also acquired.

The POM images and the reflectivity spectra of LCP (black lines) and RCP (green lines) light were taken of the center of each film, in order to characterize the structure of the film. All the solid films above display a reflected wavelength in the visible spectrum, LCP reflection and RCP transmission. The reflected spectrum of pure CNCs solid film (Figure 4.20 (a)) displays a more homogeneous reflected green coloration, since it has a low spectral width. In comparison, the sample with 2% NaFh / 98% CNCs (w/w) (Figure 4.20 (b)) has a much wider spectral meaning that reflects a broader range of colors (green and red). The last sample in Figure 4.20 (c) with 2% Cs-Ds / 98% CNC (w/w), displays a blue and green reflected coloration with a narrow width spectrum.

From these results one can conclude that by adding 2% (w/w) of Cs-Ds there is a visible regression of the reflected spectra leading to a blue and green wavelength, in contrast by adding 2% (w/w) of NaFh the reflected spectrum tends to move toward to the red wavelength.

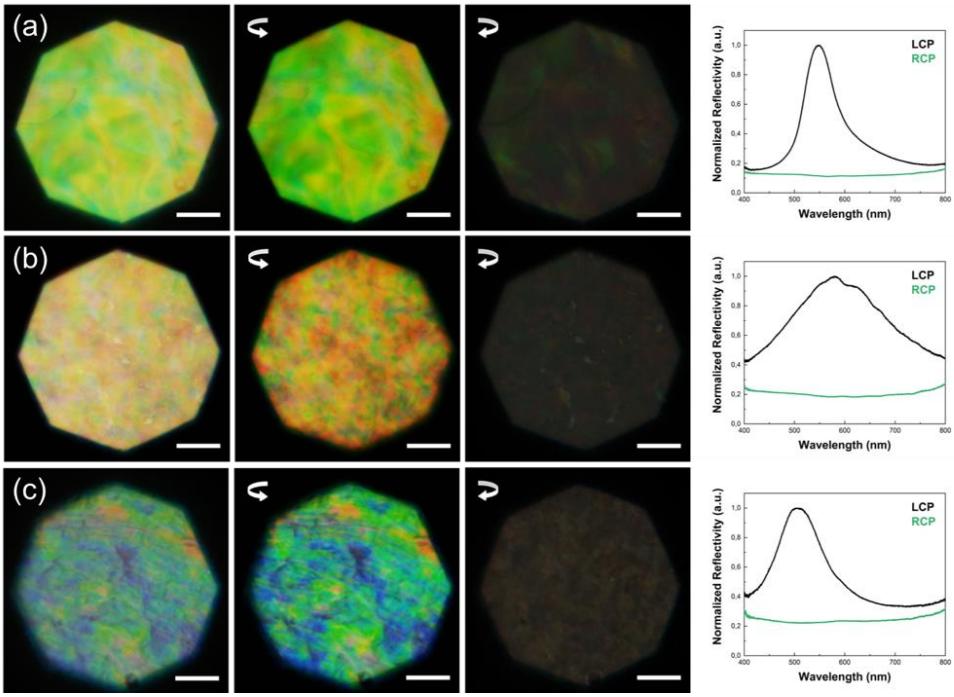

Figure 4.20 – POM images of solid films, obtained in reflection mode, in conjunction with their reflectivity spectra. (a) 100% CNCs; (b) 2% NaFh / 98% CNCs (w/w); (c) 2% Cs-Ds / 98% CNCs (w/w). Thin films were observed under left and right circularly polarized light. Scale bar (a) – (c) 50 µm.

From the spectra, in Figure 4.20, referring to the reflectivity spectra we are able to obtain the maximum wavelength peak and spectral width. Using the *de Vries* equation, Equation 1, mentioned earlier in this work, it is possible to calculate the pitch value of the samples, by dividing the wavelength peak by the refractive index of CNC (1.56) assuming that this value was not affected by the low quantity of added clay. These values are displayed in Table 5.

From the shown data, one can see that as the wavelength peak decreases the pitch value follow the same path. The spectral width of the NaFh solid film displays the highest value when compared to the other two samples, 325 nm, which is in conformity with the reflectivity spectrum and POM images that shows a defined green coloration. The film with Cs-Ds shows a decrease in the maxi-mum wavelength and in the calculated pitch when compared to the pure CNC film.

Table 5 – Maximum wavelength peak (λ_{max}), spectral width ($\Delta\lambda$) and pitch value of the solid films prepared, from CNC, CNC/NaFh and CNC/Cs-Ds.

Sample	Maximum Wavelength, λ_{max} (nm)	Spectral width, $\Delta\lambda$ (nm)	Pitch (nm)
CNC	548	112	351
CNC/NaFh	578	325	371
CNC/Cs-Ds	506	156	324

In Figure 4.21 are represented the XRD diffractograms patterns of the three solid films produced after solvent evaporation.

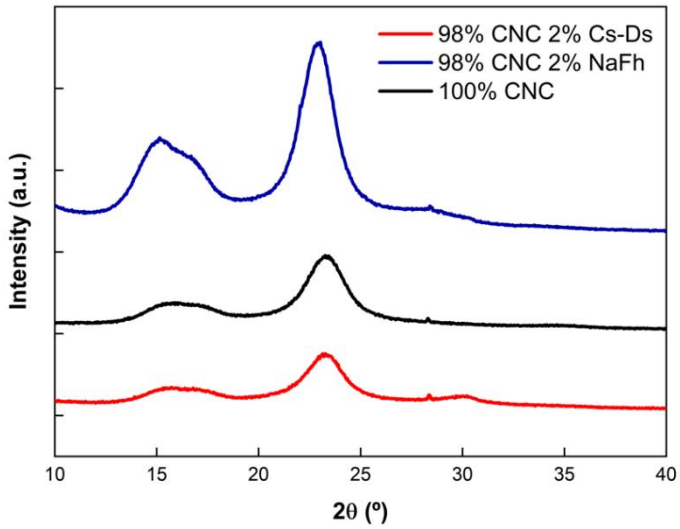

Figure 4.21 – XRD diffractograms patterns of 100% (w/w) CNCs, 98% CNCs / 2% NaFh (w/w) and 98% CNCs / 2% NaFh (w/w) solid films.

The black, blue and red lines correspond to 100% (w/w) of CNCs, 98% CNCs / 2% NaFh (w/w) and 98% CNCs / 2% Cs-Ds (w/w), respectively. All the samples show the characteristic peaks of cellulose nanocrystals at 2θ = 15 º, 16.6 º and 22.7 º which corresponds to 101, $10\bar{1}$ and 002 planes, correspondingly [51]. It can be seen that, in general, the addition of clay does not influence the composition of the solid films mixtures, since it does not change the position of the diffractograms peaks. Fact probably due to the small amount of clay added.

The FTIR spectra of the samples can be observed in Figure 4.22 which corresponds to the following: (a) 98% CNC / 2% NaFh (w/w), (b) 100% (w/w) CNC and (c) 98% CNC / 2% Cs-Ds (w/w), correspondingly. All three samples show undistinguishable FTIR spectra with absorbance bands at 3330, 2900 and 1030 cm^{-1}, which correspond to the stretching vibrations of O-H, C-H and C-O bonds [48]. In conclusion it is evident that the spectra are similar, therefore the added nanoclays did not interfere with the chemical structure of the CNC.

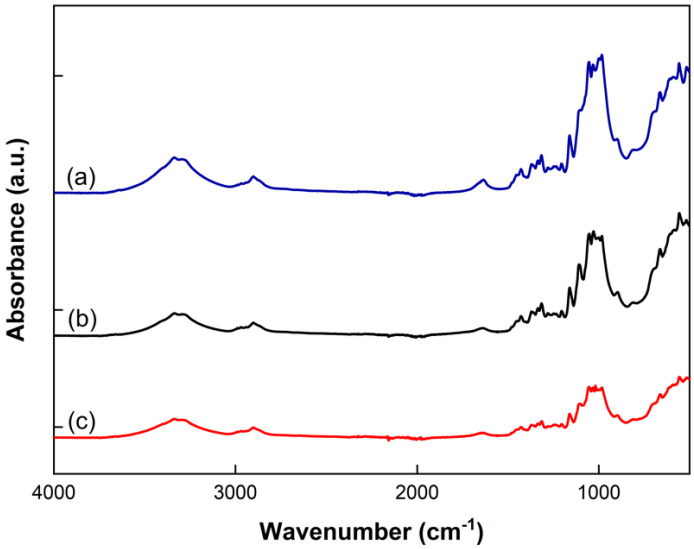

Figure 4.22 – FTIR spectra of the samples 98% CNCs / 2% NaFh (w/w) (a), 100% (w/w) CNCs (b) and 98% CNCs / 2% Cs-Ds (w/w) (c). Each individual vertical line represents an absorbance of stretching vibrations of the cellulose molecules.

The DSC-TGA analysis of pure CNCs (black lines), CNCs/NaFh (red lines) and CNCs/Cs-Ds (blue lines) is represented in the Figure 4.23.

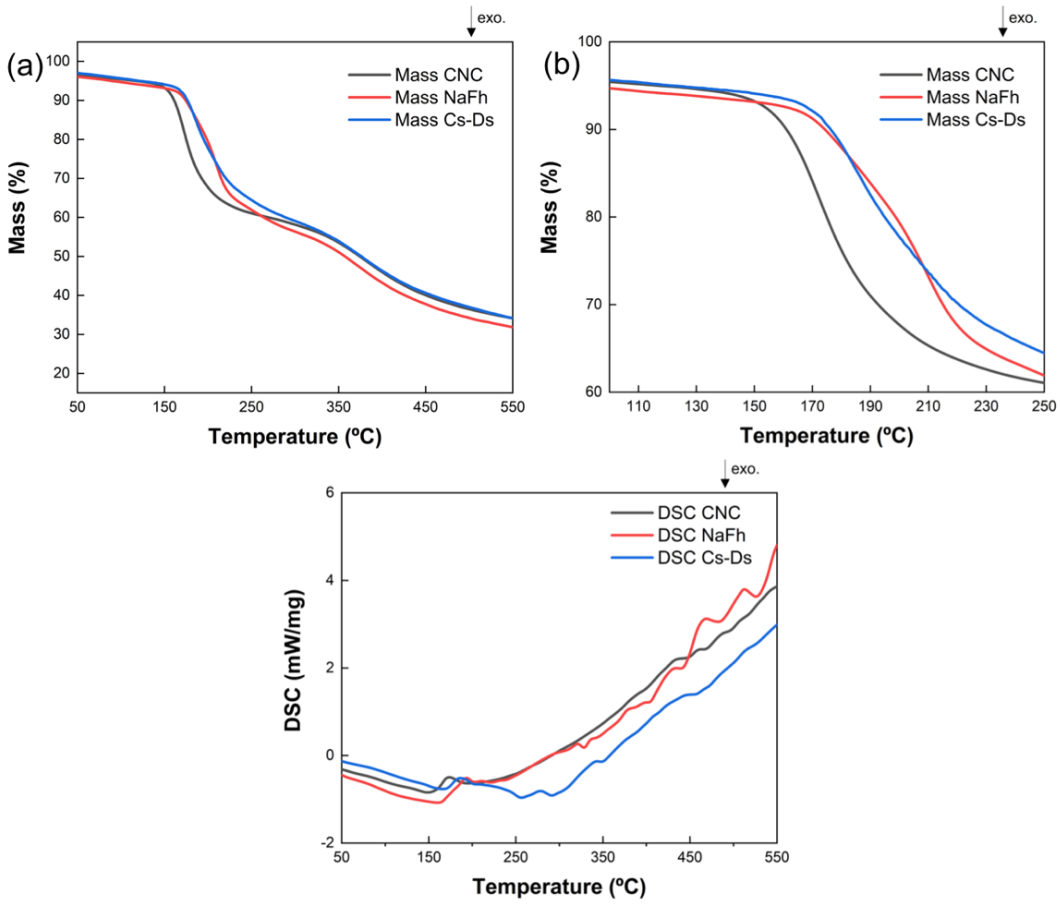

Figure 4.23 – DSC–TGA analysis of films of 100% (w/w) CNCs (black lines), 98% CNCs / 2% NaFh (w/w) (red lines) and 98% CNCs / 2% Cs-Ds (w/w) (blue lines).

With this characterization it is possible to understand the thermal stability of the produced solid films. Note that any minor mass drop before 100 ºC is due to moisture evaporation and that all three films are characterized by a second order degradation reaction that occurs between 150 ºC and 290 ºC, seen in Figure 4.23 (a).

In Figure 4.23 (b), a closer representation of the first mass drop of the samples suffered is shown. One can perceive that the film of pure CNCs is less temperature resistant to temperature, since the drop starts at 150 ºC, approximately, and has a mass loss of 36.84%. Both solid films with nanoclays and CNCs show a significantly higher resistance to temperature, as the mass drop starts at a higher temperature (170 ºC). The red and blue lines show a mass variation of 39.57% and 37.85%, respectively. These results show that the films with NaFh and Cs-Ds are more thermally stable, since the mass drop occurred at a higher temperature. This is in line with the literature which states that clay has flame retardant properties, so that the mass degradation of the film decreases with increasing percentage of clay [67].

5 Conclusion and future perspectives

The aim of this work was to produce solid films with iridescent coloration from two main raw materials widely available on earth (cellulose and clay) that would be environmentally friendly and inexpensive.

Cellulose nanocrystals were produced by acid hydrolysis of microcrystalline cellulose, using 65% (w/w) sulfuric acid, 45 ºC, 40 minutes, originating particles with an average length and width dimensions of 182 ± 34 and 4 ± 1 nm, respectively, acquired by AFM. The crystallinity index of the isolated CNCs (89.2%) has a higher value compared to CMC (75.2%). This increase is related to the removal of the amorphous regions, during the chemical process, from cellulose crystallites. The degree of substitution, of the -OSO_3H/100 anhydroglucose units, was 4.92. Five aqueous suspensions of the cellulose nanocrystals were prepared (3.03, 4.5, 5.5, 6.5 and 8.5% (w/w)) and a phase separation was observed in suspensions with a CNCs concentration ranging from 3.03 to 5.5% (w/w). As the CNCs concentration in the aqueous suspension is increased, there is a tendency for a decrease of the isotropic phase, as expected and widely investigated in previous works [61].

An aqueous suspension of a synthetic nanoclay (Sodium-Fluorohectorite), with a concentration of 1% (w/w) was mixed with the aqueous suspension of CNCs with 2.47% (w/w). Five mixed suspensions were prepared with different percentages each 99, 98, 95, 85 and 50% (w/w) of CNCs. A phase separation was observed for all prepared suspensions with concentrations below 50% (w/w) of CNCs.

Films deposited by the drop-casted method, with a percentage of 98% CNCs / 2% NaFh (w/w) were produced, by solvent evaporation technique, in different substrates (ITO with UVO treatment and microscope slides) and evaporation temperatures (4 ºC, 20 ºC and 60 ºC). It was concluded that a slower evaporation rate induced at 4 ºC, promotes the formation of thinner and homogenous films with reduction of the “coffee stain” effect, leading to a better iridescent coloration. With this study, it was possible to choose an optimal substrate (ITO with UVO treatment) and evaporation temperature (4 ºC). The profilometry scans at the highest evaporation temperature (60 ºC) showed an unusual peak at the center of the thin films, and it is suggested that the presence of clay in the cellulosic matrix affects the mobility of the crystals and alters the kinetics of the water evaporation in the thin films.

Using the optimal evaporation and colored film preparation conditions, a thin film of each suspension was prepared. It was concluded, through POM analysis that these exhibit iridescence, selective reflected left circularly polarized light and transmission of right circularly polarized light. As the percentage of NaFh increases a green shift of the reflected wavelength in the center of the thin film is noticeable, but at a percentage of 50% (w/w) of NaFh the iridescence of the thin film fades. By observing the SEM images of the cross section, it was proven that the addition nanoclay to the CNCs matrix maintained the chiral structure organizations for low concentrations of NaFh, once at 58%NaFh / 42%NCC a lamellar structure is verified.

Solid films were also prepared, by solvent evaporation technique in Petri dishes, from 2.47% (w/w) CNCs, 98% CNCs / 2% NaFh (w/w) and 98% CNCs / 2% Cs-Ds (w/w). The DSC-TGA revealed that the addition of nanoclay originated a film more thermally stable (in other words, more resistant to the temperature increase). All the produced solid films exhibit iridescence, selective reflected left circularly polarized light and transmission of right circularly polarized light, proven by POM characterization. The pure CNCs solid film, displays an iridescent green and yellow coloration and by integrating NaFh the iridescent reflected wavelength of the solid films shifts to red. On the other hand, it was observable that by combining double layer Cs-Ds clay with cellulose nanocrystals the resulting solid film displayed a bright green iridescent reflected coloration.

In conclusion, iridescent films with structural coloration were produced from aqueous CNCs/clay suspensions that preserved the selective reflection of LCP light channel. These structurally colored materials are a long run alternative to toxic chemical pigments that can be used for material surfaces or coatings due to these optical properties.

Interesting results were achieved from these studies, although better results could be achieved in the future with the following possibilities:

- Study the concentrations from which occurs structural lamellar transition to a chiral nematic organization;
- Study of the cellulose nanocrystals mixed with nanoclay cesium double layer is suggested since the obtained solid films presented very good results in terms of reflected coloration and optical response;
- Study the use of magnets, to create different magnetic fields, during the solvent evaporation process of the thin films;
- Develop further studies of CNCs from CelluForce and asses the possible replacement of synthesized CNCs.

In conjunction with the magnets, a nanoclay with magnetic nanoparticles is a very interesting future approach, since a greater alignment of the particles could be achieved.

6 References

[1] W. Herbst, K. Hunger, G. Wilker, H. Ohleier, and R. Winter, *Industrial Organic Pigments: Production, Properties, Applications: Third, Completely Revised Edition*, vol. 3. Wiley, 2004.

[2] A. P. C. Almeida, J. P. Canejo, S. N. Fernandes, C. Echeverria, P. L. Almeida, and M. H. Godinho, “Cellulose-Based Biomimetics and Their Applications,” *Advanced Materials*, vol. 30, no. 19. pp. 1–31, 2018.

[3] S. Niu *et al.*, “Excellent structure-based multifunction of morpho butterfly wings: A review,” *J. Bionic Eng.*, vol. 12, no. 2, pp. 170–189, 2015.

[4] S. Kinoshita, *Structural Colors in the Realm of Nature*, vol. 136, no. 1. Singapore: World Scientific Publishing Co. Pte. Ltd., 2008.

[5] S. Tadepalli, J. M. Slocik, M. K. Gupta, R. R. Naik, and S. Singamaneni, “Bio-Optics and Bio-Inspired Optical Materials,” *Chem. Rev.*, vol. 117, no. 20, pp. 12705–12763, 2017.

[6] S. Vergnolini *et al.*, “Pointillist structural color in Pollia fruit,” *Proc. Natl. Acad. Sci.*, vol. 109, no. 39, pp. 15712–15715, Sep. 2012.

[7] “Dogbane Beetle.” [Online]. Available: https://www.publicdomainpictures.net/en/view-image.php?image=200911&picture=dogbane-beetle-close-up. [Accessed: 10-Oct-2019].

[8] “Peacock Feathers.” [Online]. Available: https://www.publicdomainpictures.net/en/view-image.php?image=255317&picture=peacock-feathers-texture-background. [Accessed: 10-Oct-2019].

[9] “Morpho Butterfly.” [Online]. Available: https://www.publicdomainpictures.net/en/view-image.php?image=143924&picture=morpho-butterfly. [Accessed: 10-Oct-2019].

[10] J. George and S. N. Sabapathi, “Cellulose nanocrystals: Synthesis, functional properties, and applications,” *Nanotechnol. Sci. Appl.*, vol. 8, pp. 45–54, 2015.

[11] J. P. Borges, J. P. Canejo, S. N. Fernandes, P. Brogueira, and M. H. Godinho, “Cellulose-Based Liquid Crystalline Composite Systems,” *Nanocellulose Polym. Nanocomposites Fundam. Appl.*, vol. 9781118871, pp. 215–235, 2014.

[12] A. G. Dumanli *et al.*, “Controlled, bio-inspired self-assembly of cellulose-based chiral reflectors,” *Adv. Opt. Mater.*, vol. 2, no. 7, pp. 646–650, 2014.

[13] L. F. V. Pinto *et al.*, “Cellulose-Based Liquid Crystalline Photoresponsive Films with Tunable Surface Wettability,” *Langmuir*, vol. 27, no. 10, pp. 6330–6337, May 2011.

[14] G. Siqueira, J. Bras, and A. Dufresne, “Cellulosic bionanocomposites: A review of preparation, properties and applications,” *Polymers (Basel).*, vol. 2, no. 4, pp. 728–765, 2010.

[15] M. Kaushik, C. Fraschini, G. Chauve, J.-L. Putaux, and A. Moores, “Transmission Electron Microscopy for the Characterization of Cellulose Nanocrystals,” *Transm. Electron Microsc. - Theory Appl.*, 2015.

[16] NEUROtiker, “File:Cellulose Sessel.svg,” 2007. [Online]. Available: https://commons.wikimedia.org/wiki/File:Cellulose_Sessel.svg. [Accessed: 10-Oct-2019].

[17] H. Kargarzadeh, M. Ioelovich, I. Ahmad, S. Thomas, and A. Dufresne, “Methods for Extraction of Nanocellulose from Various Sources,” *Handb. Nanocellulose Cellul. Nanocomposites*, pp. 1–49, 2017.

[18] G. H. D. Tonoli *et al.*, “Cellulose micro/nanofibres from Eucalyptus kraft pulp: Preparation and properties,” *Carbohydr. Polym.*, vol. 89, no. 1, pp. 80–88, 2012.

[19] M. Shishehbor and P. D. Zavattieri, “Effects of interface properties on the mechanical properties of bio-inspired cellulose nanocrystal (CNC)-based materials,” *J. Mech. Phys. Solids*, vol. 124, pp. 871–896, 2019.

[20] M. S. Reid, M. Villalobos, and E. D. Cranston, “Benchmarking Cellulose Nanocrystals: From the Laboratory to Industrial Production,” *Langmuir*, vol. 33, no. 7, pp. 1583–1598, 2017.

[21] U. Gill, “Mechanical Properties of Cellulose Nanocrystal Thin Films,” 2017.

[22] S. Beck-Candanedo, M. Roman, and D. G. Gray, “Effect of reaction conditions on the properties and behavior of wood cellulose nanocrystal suspensions,” *Biomacromolecules*, vol. 6, no. 2, pp. 1048–1054, 2005.

[23] S. N. Fernandes *et al.*, “Mind the Microgap in Iridescent Cellulose Nanocrystal Films,” *Adv. Mater.*, vol. 29, no. 2, 2017.

[24] S. N. Fernandes *et al.*, “Structural Color and Iridescence in Transparent Sheared Cellulosic Films,” *Macromol. Chem. Phys.*, vol. 214, no. 1, pp. 25–32, 2012.

[25] A. F. Martins, “Os cristais líquidos,” *Independent*, vol. 7, p. 253, 1991.

[26] P. J. Collings and M. Hird, *Introduction to liquid crystals: Chemistry and physics*, vol. 7, no. 3. Taylor & Fancis Ltd, 2017.

[27] W. Y. Hamad, *Cellulose nanocrystals: Properties, production and applications*. John Wiley & Sons Ltd, 2017.

[28] W. Hamad, “On the Development and Applications of Cellulosic Nanofibrillar and Nanocrystalline Materials,” *Can. J. Chem. Eng.*, vol. 84, no. 5, pp. 513–519, 2006.

[29] H. de Vries, “Rotatory power and other optical properties of certain liquid crystals,” *Acta Crystallogr.*, vol. 4, no. 3, pp. 219–226, 1951.

[30] J. O. Fossum, “Physical phenomena in clays,” *Phys. A Stat. Mech. its Appl.*, vol. 270, no. 1–2, pp. 270–277, 1999.

[31] H. Hemmen *et al.*, “The isotropic-nematic interface in suspensions of na-fluorohectorite synthetic clay,” *Langmuir*, vol. 25, no. 21, pp. 12507–12515, 2009.

[32] A. Liu, A. Walther, O. Ikkala, L. Belova, and L. A. Berglund, “Clay nanopaper with tough cellulose nanofiber matrix for fire retardancy and gas barrier functions,” *Biomacromolecules*, vol. 12, no. 3, pp. 633–641, 2011.

[33] M. N. V. Prasad and K. Shih, *Environmental Materials and Waste: Resource Recovery and Pollution Prevention*. 2016.

[34] S. Farrokhpay, B. Ndlovu, and D. Bradshaw, “Behaviour of swelling clays versus non-swelling clays in flotation,” *Miner. Eng.*, vol. 96–97, pp. 59–66, 2016.

[35] F. Bergaya and G. Lagaly, “General introduction: Clays, clay minerals, and clay science,” *Dev. Clay Sci.*, vol. 1, pp. 1–18, 2006.

[36] L. Valdés, I. Pérez, L. C. De Ménorval, E. Altshuler, J. O. Fossum, and A. Rivera, “A simple way for targeted delivery of an antibiotic: In vitro evaluation of a nanoclay-based composite,” *PLoS One*, vol. 12, no. 11, 2017.

[37] K. S. Novoselov, A. Mishchenko, A. Carvalho, and A. H. Castro Neto, “2D materials and van der Waals heterostructures,” *Science (80-.).*, vol. 353, no. 6298, Jul. 2016.

[38] M. Daab *et al.*, “Onset of Osmotic Swelling in Highly Charged Clay Minerals,” *Langmuir*, vol. 34, no. 28, pp. 8215–8222, Jul. 2018.

[39] E. DiMasi, J. O. Fossum, T. Gog, and C. Venkataraman, “Orientational order in gravity dispersed clay colloids: A synchrotron x-ray scattering study of Na fluorohectorite suspensions,” *Phys. Rev. E*, vol. 64, no. 6, p. 061704, Nov. 2001.

[40] H. Hemmen, L. R. Alme, J. O. Fossum, and Y. Meheust, “X-ray studies of interlayer water absorption and mesoporous water transport in a weakly hydrated clay,” *Phys. Rev. E - Stat. Nonlinear, Soft Matter Phys.*, vol. 82, no. 3, pp. 1–11, 2010.

[41] D. M. Fonseca, Y. Méheust, J. O. Fossum, K. D. Knudsen, and K. P. S. Parmar, “Phase diagram of polydisperse Na-fluorohectorite-water suspensions: A synchrotron small-angle x-ray scattering study,” *Phys. Rev. E - Stat. Nonlinear, Soft Matter Phys.*, vol. 79, no. 2, pp. 1–11, 2009.

[42] A. Lerf, “Storylines in intercalation chemistry,” *Dalt. Trans.*, vol. 43, no. 27, pp. 10276–10291, 2014.

[43] V. Nicolosi, M. Chhowalla, M. G. Kanatzidis, M. S. Strano, and J. N. Coleman, “Liquid exfoliation of layered materials,” *Science (80-.).*, vol. 340, no. 6139, pp. 72–75, 2013.

[44] H. Hemmen, E. L. Hansen, N. I. Ringdal, and J. O. Fossum, “The frederiks transition in an aqueous clay dispersion,” *Rev. Cuba. Fis.*, vol. 29, no. 1E, pp. 59–61, 2012.

[45] J. F. Revol, H. Bradford, J. Giasson, R. H. Marchessault, and D. G. Gray, “Helicoidal self-ordering of cellulose microfibrils in aqueous suspension,” *Int. J. Biol. Macromol.*, vol. 14, no. 3, pp. 170–172, 1992.

[46] M. Stöter *et al.*, “Nanoplatelets of Sodium Hectorite Showing Aspect Ratios of ≈20 000 and Superior Purity,” *Langmuir*, vol. 29, no. 4, pp. 1280–1285, Jan. 2013.

[47] J. Breu, W. Seidl, A. J. Stoll, K. G. Lange, and T. U. Probst, “Charge homogeneity in synthetic fluorohectorite,” *Chem. Mater.*, vol. 13, no. 11, pp. 4213–4220, 2001.

[48] M. G. Aguayo *et al.*, “Isolation and characterization of cellulose nanocrystals from rejected fibers originated in the Kraft Pulping process,” *Polymers (Basel).*, vol. 10, no. 10, 2018.

[49] I. K. I. Al-khateeb, S. M. Hussin, and Y. M. Al-obaidi, “Extraction of Cellulose Nano Crystalline from Cotton by Ultrasonic and Its Morphological and Structural Characterization,” *Int. J. Mater. Chem. Phys.*, vol. 1, no. 2, pp. 99–109, 2015.

[50] D. Gaspar *et al.*, “Nanocrystalline cellulose applied simultaneously as the gate dielectric and the substrate in flexible field effect transistors,” *Nanotechnology*, vol. 25, no. 9, p. 094008, Mar. 2014.

[51] I. Carrillo, R. T. Mendonça, M. Ago, and O. J. Rojas, “Comparative study of cellulosic components isolated from different Eucalyptus species,” *Cellulose*, vol. 25, no. 2, pp. 1011–1029, 2018.

[52] D. Klemm, B. Heublein, H. P. Fink, and A. Bohn, “Cellulose: Fascinating biopolymer and sustainable raw material,” *Angew. Chemie - Int. Ed.*, vol. 44, no. 22, pp. 3358–3393, 2005.

[53] L. Segal, J. J. Creely, A. E. Martin, and C. M. Conrad, “An Empirical Method for Estimating the Degree of Crystallinity of Native Cellulose Using the X-Ray Diffractometer,” *Text. Res. J.*, vol. 29, no. 10, pp. 786–794, 1959.

[54] N. F. Vasconcelos *et al.*, “Bacterial cellulose nanocrystals produced under different hydrolysis conditions: Properties and morphological features,” *Carbohydr. Polym.*, vol. 155, pp. 425–431, 2017.

[55] Roman. M and Winter. WT, “Effect of Sulfate Groups from Sulfuric Acid Hydrolysis on the Thermal Degradation Behavior of Bacterial Cellulose,” *Biomacromolecules*, vol. 5, pp. 1671–1677, 2004.

[56] M. A. Mohamed, W. N. W. Salleh, J. Jaafar, S. E. A. M. Asri, and A. F. Ismail, “Physicochemical properties of ‘green’ nanocrystalline cellulose isolated from recycled newspaper,” *RSC Adv.*, vol. 5, no. 38, pp. 29842–29849, 2015.

[57] S. Elazzouzi-Hafraoui, Y. Nishiyama, J. L. Putaux, L. Heux, F. Dubreuil, and C. Rochas, “The shape and size distribution of crystalline nanoparticles prepared by acid hydrolysis of native cellulose,” *Biomacromolecules*, vol. 9, no. 1, pp. 57–65, 2008.

[58] J. L. Huang, C. J. Li, and D. G. Gray, “Cellulose nanocrystals incorporating fluorescent methylcoumarin groups,” *ACS Sustain. Chem. Eng.*, vol. 1, no. 9, pp. 1160–1164, 2013.

[59] W. Y. Hamad and T. Q. Hu, “Structure-process-yield interrelations in nanocrystalline cellulose extraction,” *Can. J. Chem. Eng.*, vol. 88, no. 3, pp. 392–402, 2010.

[60] I. Hoeger, O. J. Rojas, K. Efimenko, O. D. Velev, and S. S. Kelley, “Ultrathin film coatings of aligned cellulose nanocrystals from a convective-shear assembly system and their surface mechanical properties,” *Soft Matter*, vol. 7, no. 5, pp. 1957–1967, 2011.

[61] C. Honorato-Rios, A. Kuhnhold, J. R. Bruckner, R. Dannert, T. Schilling, and J. P. F. Lagerwall, “Equilibrium liquid crystal phase diagrams and detection of kinetic arrest in cellulose nanocrystal suspensions,” *Front. Mater.*, vol. 3, no. May, pp. 1–13, 2016.

[62] P.-X. Wang, W. Y. Hamad, and M. J. MacLachlan, “Structure and transformation of tactoids in cellulose nanocrystal suspensions,” *Nat. Commun.*, vol. 7, no. 1, p. 11515, Sep. 2016.

[63] P. Kuang, J. H. Lee, C. H. Kim, K. M. Ho, and K. Constant, “Improved surface wettability of polyurethane films by ultraviolet ozone treatment,” *J. Appl. Polym. Sci.*, vol. 118, no. 5, pp. 3024–3033, Dec. 2010.

[64] A. G. Dumanli *et al.*, “Digital Color in Cellulose Nanocrystal Films,” *ACS Appl. Mater. Interfaces*, vol. 6, no. 15, pp. 12302–12306, Aug. 2014.

[65] R. D. Deegan, O. Bakajin, T. F. Dupont, G. Huber, S. R. Nagel, and T. A. Witten, “Capillary flow as the cause of ring stains from dried liquid drops,” *Nature*, vol. 389, no. 6653, pp. 827–829, Oct. 1997.

[66] J. Breu, W. Seidl, A. J. Stoll, K. G. Lange, and T. U. Probst, “Charge Homogeneity in Synthetic Fluorohectorite,” *Chem. Mater.*, vol. 13, no. 11, pp. 4213–4220, Nov. 2001.

[67] C. D. Delhom, L. A. White-Ghoorahoo, and S. S. Pang, “Development and characterization of cellulose/clay nanocomposites,” *Compos. Part B Eng.*, vol. 41, no. 6, pp. 475–481, 2010.

[68] C. M. Ewulonu, G. C. Emeh, M. C. Njoku, and D. C. Ugwuegbu, “Evaluating the Surface Coating Potentials of South-Eastern Nigeria Local Clays in Alkyd Paints,” vol. 1, no. 2, pp. 10–20, 2016.

[69] N. Cruz and Y. Peng, “Rheology measurements for flotation slurries with high clay contents – A critical review,” *Miner. Eng.*, vol. 98, pp. 137–150, Nov. 2016.

7 Supporting information

7.1 AFM measurements of length and width of CNCs Avicel®

Table 6 – AFM measurements of both length and width of the produced CNCs.

		a	b	c	d	e	f	g	h	i	j
Length (nm)	1	225.57	174.35	200.40	163.20	146.58	182.92	173.35	214.68	118.64	175.24
	2	224.78	150.29	190.52	222.08	150.41	208.05	169.63	185.81	155.43	182.60
	3	194.53	146.70	189.57	172.81	140.14	212.04	143.31	187.00	122.18	225.41
	4	214.58	182.70	229.91	187.71	207.85	176.85	199.15	182.92	168.63	171.27
	5	268.53	143.80	205.64	217.23	151.96	217.47	208.45	179.37	205.45	129.34
	6	244.69	194.21	231.76	229.87	166.67	157.67	173.02	165.17	196.98	136.68
	7	208.56	137.72	167.92	162.98	165.17	172.81	244.36	232.92	170.54	162.00
	8	207.88	160.60	188.06	201.92	193.64	207.45	166.67	138.62	167.92	192.52
	9	172.81	181.82	158.68	255.80	131.38	132.23	176.97	181.82	174.58	166.03
	10	248.48	181.51	169.83	266.79	170.62	164.53	222.50	168.52	160.01	152.66
	11	196.62	182.12	197.81	157.92	158.37	185.09	148.95	149.07	171.89	198.73
	12	189.47	183.76	179.24	163.85	141.62	247.71	187.78	159.35	143.03	205.64
	13	193.64	226.88	158.34	233.25	124.41	265.61	173.56	160.43	177.80	133.53
	14	190.03	164.93	261.16	251.38	185.09	177.00	205.19	152.20	239.68	121.27
	15	171.86	258.63	147.16	177.00	129.34	162.22	166.11	143.31	250.88	149.43
Width (nm)	1	6.06	5.43	4.43	5.68	4.43	5.29	3.29	3.43	5.41	6.00
	2	4.64	3.87	3.96	4.00	3.45	5.00	3.59	5.78	4.58	4.03
	3	4.67	4.72	4.21	4.94	6.10	4.06	5.37	6.22	4.62	4.08
	4	2.62	6.54	4.06	3.54	4.72	4.80	3.95	3.94	4.88	4.54
	5	4.14	4.28	6.11	5.02	4.95	3.29	3.57	3.88	4.57	3.39
	6	4.16	2.51	5.37	4.39	5.52	4.25	3.68	4.41	4.80	4.12
	7	2.85	5.27	4.81	5.15	3.05	4.54	4.18	4.77	4.54	5.71
	8	4.35	3.77	3.58	4.66	4.91	4.00	4.35	4.07	4.72	4.62
	9	4.11	4.26	4.60	3.86	4.80	7.28	4.42	3.32	3.88	3.61
	10	3.85	4.35	4.40	5.42	3.29	5.07	5.80	5.69	4.42	4.14
	11	3.24	4.27	6.13	5.78	2.93	5.17	3.56	4.73	5.69	4.47
	12	3.91	5.01	5.04	4.46	3.70	3.67	4.82	4.48	4.36	4.57
	13	4.39	4.35	4.68	3.74	3.98	4.68	3.71	5.75	5.99	3.79
	14	3.96	3.68	4.48	3.16	3.78	3.62	4.13	3.77	3.58	5.16
	15	3.44	4.32	5.01	3.46	3.32	5.20	5.42	4.69	4.35	3.79

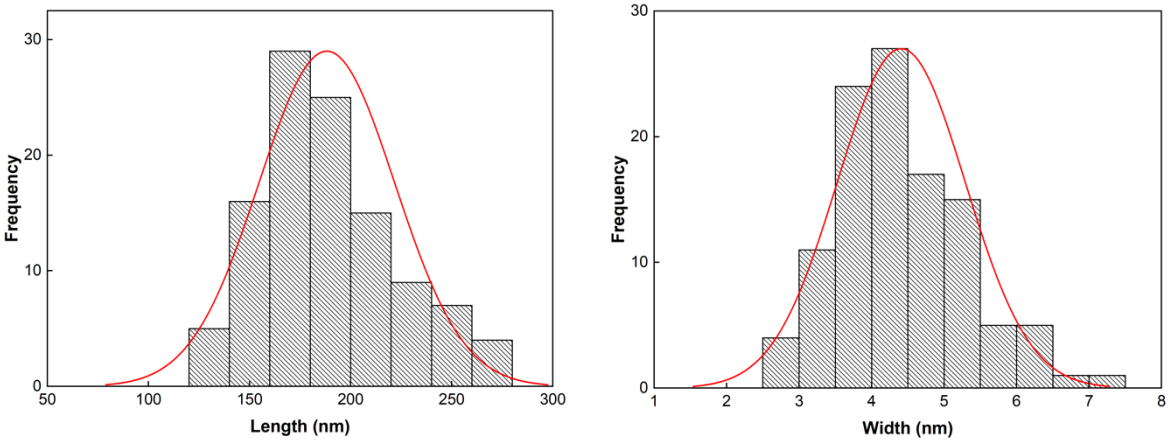

Figure 7.1 – Distribution of CNCs Avicel® particles measurements of length and width represented in a histogram.

7.2 Thickness measurements of solid films

Table 7 – Thickness measurements of solid films of pure CNCs, CNCs with NaFh and CNCs with Cs-Ds.

		CNCs	CNCs/NaFh	CNCs/Cs-Ds
Thickness (µm)	**1**	21	31	20
	2	33	40	19
	3	26	30	21
	4	29	33	36
	5	28	27	25
	6	26	30	14
	7	21	33	21
	8	23	29	22
	9	27	44	19
	10	26	34	34

7.3 CNCs CelluForce®

In addition, to the CNCs that was synthesized in the laboratory, a commercial nanocrystalline cellulose for future testing was prepared (CelluForce NCC®, CAS# 9005-22-5, 100% (w/w)). From these CNCs a aqueous suspension was prepared, by diluting the CNCs in ultrapure water. This suspension had a concentration of 5% (w/w) and a volume of 15 g. The resulting material was dispersed by magnetic agitation for 2 hours. Lastly the suspension was sonicated during 56

minutes (using a VC 505 from Sonics®), with magnetic agitation at 0.5 of the cycle and 60% amplitude (applying 4053 Joules in total). The suspension was left in a cold environment (4 ºC), for 1 week, in order to achieve visible phase separation. In the literature several comparisons between CNCs produced laboratory and industrially have been published. Reid *et al.* reported that overall the cellulose nanocrystals from CelluForce compare well with lab produced CNCs. Although some differences in the sulfate half-ester content, colloidal stability, crystallinity and morphology were verified [20].

The dimensions of “rice-like” structures from the prepared CNCs suspension was characterized by AFM (Figure 7.2).

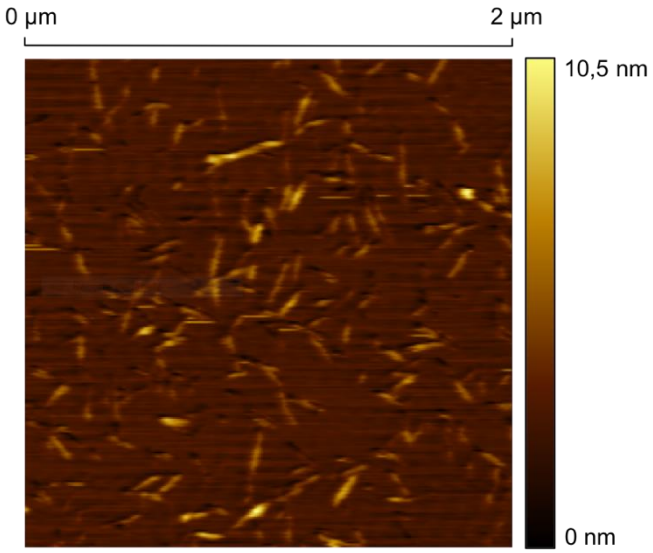

Figure 7.2– AFM image, in amplitude retrace mode, of a diluted aqueous CNCs suspension. Window dimensions: 2 µm by 2 µm.

The acquired AFM image shows a dehydrated droplet, of the diluted, 0.0025% (w/w), aqueous CNCs suspension. In order to assess the dimensions (length and width), 105 measurements were made using the Gwyddion software. The mean value of the length and width measured are 176 ± 36 nm and 6 ± 1 nm, respectively, which corresponds to an aspect ratio of 29. The obtained values are within the ones presented by Cranston and co-workers for CelluForce (183 ± 88 nm and 6 ± 2 nm for average length and width, respectively, and a 31 ratio) [20]. Additional information, such as tables and distribution graphs, regarding the AFM measurements can be found in the supporting information 7.4.

Using 2 ml of the CNCs aqueous suspension, a solid films was casted by solvent evaporation method in a Petri dish (35 mm diameter) at a temperature of 4 ºC, Figure 7.3.The thickness of the solid film is 62 ± 4 nm, which is much higher value when compared to the solid films produced earlier in this work.

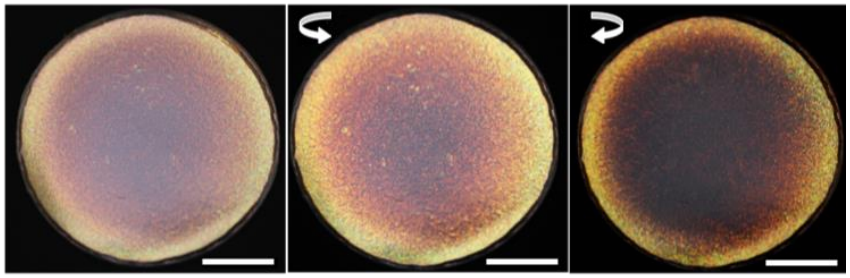

Figure 7.3 – Macroscopic photographic images of a solid film from pure CNCs. The solid film was observed under left and right circularly polarized light. Scale bar 1 cm.

Observing the macroscopic images, a bright red reflected coloration is displayed in the left circularly polarized light. The image corresponding to the RCP channel shows that the center of the solid film transmits all the light and the outer edge fails to transmit all the light.

7.4 AFM measurements of length and width of CNCs CelluForce®

Table 8 – Thickness measurements of solid films of CNCs from CelluForce®

		a	b	c	d	e	f	g
Length (nm)	**1**	164.61	190.49	255.26	195.86	147.52	194.29	178.39
	2	144.61	216.23	262.70	146.05	183.85	184.93	135.64
	3	164.43	175.29	164.38	179.57	190.77	136.59	153.08
	4	137.83	179.52	149.92	185.76	150.49	158.24	176.83
	5	156.62	175.26	269.58	192.91	157.43	155.84	185.81
	6	180.64	299.20	236.14	172.82	164.95	224.87	165.50
	7	162.36	128.23	175.02	110.64	151.19	120.65	137.24
	8	138.54	205.36	123.86	160.95	208.48	171.64	130.45
	9	129.70	190.09	177.78	257.14	177.34	151.77	184.86
	10	132.60	161.96	185.99	177.07	173.79	175.45	184.83
	11	182.58	161.15	247.49	159.26	188.66	186.07	202.12
	12	105.98	185.07	154.83	123.65	155.31	186.61	218.90
	13	205.64	291.33	188.99	161.55	162.48	188.00	204.83
	14	208.64	221.84	168.21	187.32	140.65	121.30	199.77
	15	143.04	165.54	141.02	163.40	113.44	145.58	176.04
Width (nm)	**1**	6.41	7.80	4.60	5.41	5.69	4.03	4.44
	2	5.93	4.12	3.93	7.02	5.06	4.73	4.86
	3	4.96	5.04	5.92	6.13	5.10	4.23	7.15
	4	5.56	4.70	4.83	5.50	5.84	4.21	6.89
	5	6.17	5.30	7.04	7.33	5.88	4.80	6.65
	6	5.32	6.24	5.83	5.20	8.08	6.82	7.37
	7	4.90	4.05	4.83	5.95	5.25	4.96	6.77
	8	8.31	5.60	4.21	5.52	5.71	4.10	7.02
	9	7.52	4.74	4.61	5.51	4.43	3.38	6.74
	10	7.19	6.17	6.37	6.07	6.06	4.66	6.78
	11	4.87	7.06	5.03	4.33	5.53	3.92	6.64
	12	8.06	5.05	5.94	5.76	3.05	5.05	6.73
	13	6.06	5.79	5.79	6.12	4.74	5.41	6.92
	14	4.42	5.42	5.89	6.02	4.81	4.55	7.21
	15	4.65	3.45	6.68	4.86	3.89	3.80	6.97

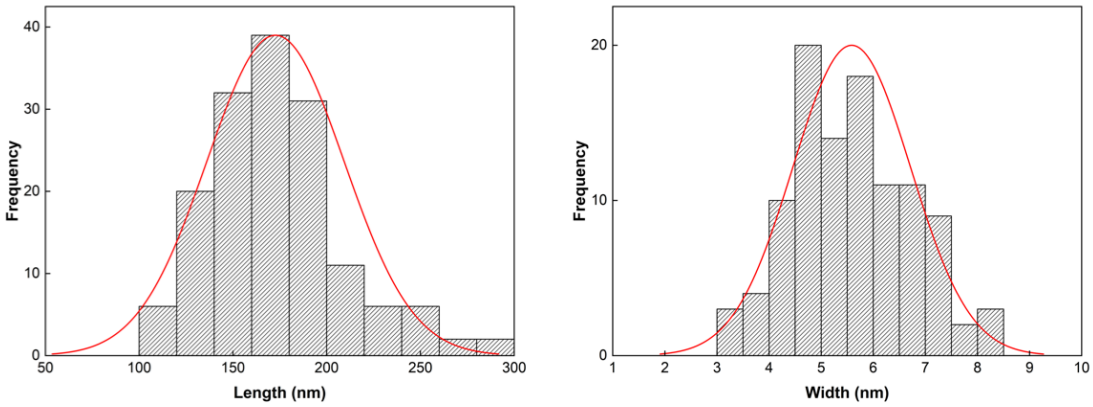

Figure 7.4 – Distribution of CNCs CelluForce® particles measurements of length and width represented in a histogram.